Master of Science

An investigation into the enhancement of g-C_3N_4 photocatalytic performance by surface modification

The Graduate School of the University of Ulsan

Department of Chemical Engineering

Hoang Thi Van Anh

An investigation into the enhancement of g-C_3N_4 photocatalytic performance by surface modification

Supervisor: Professor Eun Woo Shin

A Dissertation

Submitted to

The Graduate School of the University of Ulsan

In Partial Fulfillment of the Requirements for the Degree of

Master of Science

By

Hoang Thi Van Anh

Department of Chemical Engineering

University of Ulsan, Korea

June 2023

An investigation into the enhancement of g-C_3N_4 photocatalytic performance by surface modification

This certifies that the master's thesis of Hoang Thi Van Anh is approved

_____

Committee Chair Prof. Sung Gu Kang

_____

Committee Chair Prof. Won Mook Choi

_____

Committee Chair Prof. Eun Woo Shin

Department of Chemical Engineering

University of Ulsan, Korea

June 2023

ACKNOWLEDGEMENT

It would be my pleasure to take this opportunity to express my thankfulness to every who supported me in finishing my thesis.

First and foremost, I would like to express my appreciation to my supervisor, Professor. Eun Woo Shin for his great expertise and guidance throughout the research process. His insightful advice and feedback have improved my thinking and are valuable to my research.

I would like to show my gratitude to all my committee members Professor Sung Gu Kang and Professor Won Mook Choi, who offered insightful criticism and support throughout the thesis defense.

Furthermore, I am thankful to Mrs. Kyung Jo Lim and all staff members of the Department of Chemical Engineering for their dedication and collaboration. In addition to these thank you notes, I would like to express my gratitude to my labmates Ms. Nguyen Thi Kim Anh, Mr. Sang Yoon Kim, Mr. Dao Duc Quang, Mr. Nguyen Phuong Anh, Ms. Mingyan Wang, Dr. Azam Jamsaz, and Mr. Pham Ngoc Nhiem for their great support and friendship.

Finally, I would like to acknowledge the encouragement and support I have received from family and my friends in the Department of Chemical Engineering and from other Departments at the University of Ulsan, which has been a valuable source of inspiration for me.

ABSTRACT

In this work, the enhancement of g-C_3N_4 photocatalytic performance by surface modification was investigated for two applications: photodegradation of tetracycline hydrochloride (TC) and photocatalytic hydrogen evolution.

To study the effect of g-C_3N_4 on the photodegradation of TC, g-C_3N_4 samples were prepared by the hydrothermal process with different hydrolysis times and temperatures, namely CN-180-x and CN-200-6 and characterized by multiple physicochemical techniques. Compared to the CN, CN-180-6 possesses remarkable photocatalytic degradation efficiency at 97.17% towards TC removal in an aqueous solution. The high visible-light-induced photo-reactivity of CN-180-6 directly correlates to charge transfer efficiency, numerous structural defects with a high specific surface area, and sufficient O-functional groups over g-C_3N_4. However, hydrothermal treatment at a higher temperature or for a longer time additionally induces the growth of extended melem units on the surface of g-C_3N_4, resulting in the inhibition of the charge transfer.

The hydrogen evolution production was enhanced through the synthesis of g-C_3N_4 catalysts co-doped with oxygen (O) and phosphorus (P). By using the doping process, controlled amounts of O-groups could be introduced into g-C_3N_4 without the growth of melem units as is the case with hydrothermal treatment. Furthermore, the substitution of nitrogen with P and O added into g-C_3N_4 enabled the separation of photogenerated charge carriers, inhibited the recombination of electron-hole pairs, and assisted the formation of Pt^{2+} for hydrogen evolution. As a result, $O_{2.5}$-PCN_UPt showed the highest hydrogen evolution performance at 439.7 μmol. $g^{-1}.h^{-1}$.

CONTENTS

Acknowledgement i

Abstract ii

Contents iii

List of figures v

List of tables vii

Nomenclatures viii

Chapter 1. Introduction 1

1.1 Graphitic Carbon Nitride – based photocatalysis 1

1.2 Hydrothermal method 2

1.3 Doping method 2

1.4 Photodegradation of tetracycline hydrochloride antibiotic 3

1.5 Water splitting photocatalyst for H_2 evolution reaction 4

1.6 Research objectives 6

Chapter 2. Materials and Method 7

2.1 Catalyst preparation 7

2.2 Characterization 9

2.3 Photocatalytic activity 10

2. 3. 1 Photodegradation test 10

2. 3. 2 H_2 evolution reaction test 11

Chapter 3. Results and Discussion 12

3.1 The growth of extended melem units 12

3. 1. 1 Physicochemical properties 12

3. 1. 2 Optical properties of modified g-C_3N_4 19

3. 1. 3 Photodegradation performance 22

3. 1. 4 Conclusion 27

3.2 The O and P co-doped effect on the H_2 evolution reaction 28

3. 2. 1 Physicochemical and morphological properties 28

3. 2. 2 Optical properties of modified O_yPCN_UPt 37

3. 2. 3 H_2 evolution performance 41

3. 2. 4 Conclusion 43

Chapter 4. Conclusion 44

References 45

LIST OF FIGURES

Figure 1. Tetracycline Hydrochloride structure. 4

Figure 2. The Global total consumption by source and CO_2 emissions from fuel combustion in 2019 [43] 5

Figure 3. The synthesis of CN, CN-180-x, and CN-200-6..... 7

Figure 4. The synthesis of $OyPCN_UPt$ catalysts..... 8

Figure 5. N_2 adsorption/desorption isotherms of as-prepared photocatalysts. 13

Figure 6. TEM images of CN-180-3 (a), CN-180-6 (b,e), CN-180-9 (c), and CN-200-6 (d). 14

Figure 7. (A) XRD patterns and (B) FT-IR spectra of CN-180-x and CN-200-6 samples. 16

Figure 8. XPS data of C 1s, N 1s, and O 1s for all the photocatalysts. 18

Figure 9. (A) UV–Vis DRS absorption spectra, (B) Tauc plots for the band gap, (C) the EIS Nyquist plots, and (D) time-resolved fluorescence decay spectra in the ns time scale with excitation 400 nm (inset table: the calculated average fluorescence lifetime (τ_{av})) of as-synthesized CN-180-x and CN-200-6 samples. 20

Figure 10. Band diagrams of the CN-180-x and CN-200-x photocatalysts. 21

Figure 11. Photodegradation efficiency of TC by CN-180-x and CN-200-6 under visible light irradiation (140W xenon lamp, $\lambda > 420$nm) (A) C/C_0 vs. t (Initial condition: 20 mg L^{-1} TC, 0.2 g L^{-1} catalyst, pH = 4.40, 20°C), and (B) TC removal efficiency (%)..... 23

Figure 12. (A) The pseudo-first-order reaction kinetics and (B) rate constants (k) of as-prepared photocatalysts for TC photodegradation. 25

Figure 13. Recycling ability evaluation of CN-180-6. 26

Figure 14. The influence of reactive species on TC removal efficiency (%). 27

Figure 15. The N_2 adsorption-desorption isotherm and the corresponding pore diameter distribution (insert) of photocatalysts. 29

Figure 16. (A) FT-IR spectra and (B) XRD patterns of photocaalysts. 31

Figure 17. FE-SEM images of CN_UPt (a,b), $O_{1.5}PCN_UPt$ (c,d), $O_{2.5}PCN_UPt$ (e,f), and $O_{3.5}PCN_UPt$ (g,h). 33

Figure 18. STEM images and Pt diameter (nm) of CN_UPt (a), $O_{1.5}PCN_UPt$ (b), $O_{2.5}PCN_UPt$ (c), and $O_{3.5}PCN_UPt$ (d). 34

Figure 19. XPS data of C 1s, N 1s, O 1s, P 2p, and Pt 4f for all the photocatalysts. 36

Figure 20. Atomic percentage (at.%) of (A) O-containing functional groups and (B) Pt valence state. 37

Figure 21. (A) UV–Vis DRS absorption spectra, (B) Tauc plots for the band gap, (C) the PL spectra, and (D) the EIS Nyquist plots of O_yPCN_UPt photocatalysts. 39

Figure 22. (A) XPS-VB spectra and (B) band structure diagram of the synthesized samples. 40

Figure 23. (A) Hydrogen evolution performance (µmol. g^{-1}), (B) Hydrogen evolution rate (µmol. $g^{-1}.h^{-1}$) of O_yPCN_UPt, and (C) recycle test of $O_{2.5}PCN_UPt$. 42

Figure 24. A schematic formation of CNuPt, $O_{2.5}PCN_UPt$, and $O_{3.5}PCN_UPt$ (before and after Pt loading). 43

LIST OF TABLES

Table 1. Specific surface area, pore volume, and average pore size of photocatalysts were determined via N_2 adsorption-desorption isotherm measurements. 13

Table 2. C/N and O/N atomic ratios of all prepared samples were obtained from elemental analysis. 18

Table 3. Kinetic rate constants (k) and correlation coefficients (r^2) of TC photodegradation..... 24

Table 4. Specific surface area, pore volume, and average pore diameter of all synthesized samples were determined via N_2 adsorption-desorption isotherm measurements. 29

Table 5. N, C, O, and Pt content (wt.%), and the atomic ratio of photocatalysts. 35

Table 6. Fitted parameters of CN_UPt, $O_{1.5}PCN_UPt$, $O_{2.5}PCN_UPt$, and $O_{3.5}PCN_UPt$ for the Nyquist plots. 40

NOMENCLATURES

TC: Tetracycline Hydrochloride

EJ: Exajoules

Mt: Million tonnes

XRD: X-ray diffraction

BET: Brunauer – Emmett – Teller

FTIR: A Fourier transform infrared

TEM: Transmission electron microscopy

FE-SEM: Field-emission scanning electron microscopy

UV-Vis DRS: Ultraviolet-visible diffuse reflectance spectroscopy

PL: Photoluminescence

TRPL: Time-resolved photoluminescence

EIS: Electrochemical impedance spectroscopy

R_s: Solution resistance

R_{ct}: Charge transfer resistance

C_1: Capacity of double layer

C_2: Mass transfer control

Chapter 1. INTRODUCTION

1.1 Graphitic Carbon Nitride – based photocatalysis

In recent years, among a numerous number of semiconductors photocatalysts, graphitic carbon nitride (g-C_3N_4) has accumulated significant interdisciplinary attention as an organic, n-type visible-light active photocatalyst due to its specific characteristics and potential applications in different areas. g-C_3N_4 is a polymeric material composed of nitrogen and carbon atoms arranged in a two-dimensional layered structure similar to graphene. However, the difference between g-C_3N_4 and graphene is the inclusion of C-N bonds in g-C_3N_4 and sp^2 hybridization. Besides, basic atomic structures in g-C_3N_4 are characterized by the periodic arrangement of the tri-s-triazine motif within the plane, as well as the packing of the structural aromatic systems between layers. Generally, g-C_3N_4 is synthesized via the pyrolysis of organic substances containing both carbon and nitrogen, such as urea, thiourea, melamine, and ethylene diamine.

Owing to its excellent photocatalytic characteristics, g-C_3N_4 is a material that offers several advantages, demonstrating it is a promising candidate for a wide range of applications [1-5]. Notably, among these advantages is its exceptional photocatalytic activity, the well-known metal-free semiconductor g-C_3N_4 has been indicated as a promising material for photocatalysis due to its suitable band gap (2.7 eV) for visible light particularly [6-8]. Furthermore, the bandgap of g-C_3N_4 can be controlled by adjusting its chemical structure and composition, thus optimizing it for specific applications [9, 10]. Additionally, g-C_3N_4 is characterized by chemical and thermal stability, and ecological friendliness, and has a relatively low cost compared to other semiconductors [11-13].

Although enormous efforts have been made in various ways to utilize photocatalysts, there are still many challenging problems in the photocatalytic performance of g-C_3N_4. One of these drawbacks is its low specific surface area, which reduces the ability for adsorption and photocatalysis [14]. Furthermore, the low separation and high recombination rate of photogenerated charge carriers inhibit the photocatalytic performance of g-C_3N_4 [15, 16]. Its hydrophobic surface also inhibits the adsorption of water molecules, which in turn hinders its efficiency to facilitate the splitting of water molecules or the degradation of pollutants [17, 18]. To overcome these issues,

numerous attempts have been made to facilitate the photocatalytic behavior of g-C_3N_4 via heterostructure construction [19, 20], defects engineering [21, 22], and doping technology [23-25].

1.2 Hydrothermal method

The defect modification of g-C_3N_4 has been extensively employed to significantly enhance its photocatalytic performance [26-29]. In terms of the enhancement of the overall performance of materials, the hydrothermal process has been introduced as an effective and uncomplicated method to significantly improve the photocatalytic properties of the g-C_3N_4 photocatalyst. This facile and green method can etch numerous defects on the g-C_3N_4 surface and introduce desirable O-containing functional groups to improve photodegradation efficiency [7, 30]. Hoang et al. prepare synthesized g-C_3N_4 material through solvothermal treatment including O-functional groups, which facilitated the defect on the g-C_3N_4 surface [7]. While Hou et al. suggest that the O-doped g-C_3N_4 and defect engineering by the hydrothermal process can enhance the charge separation and inhibit the recombination of electron-hole pairs, which increases the photocatalytic activity of g-C_3N_4 [30]. However, it was reported that strong hydrolysis in the method also degraded a regular array of tri-s-triazine (melem) units in the g-C_3N_4 structure [30]. To the best of our knowledge, there have been no reports on the effects of extended melem unit formation on g-C_3N_4 via hydrothermal treatment.

1.3 Doping method

The doping method is one of the most advantageous approaches to incorporate foreign atoms or molecules into the g-C_3N_4 crystal lattice structure to modify the energy band structure and electronic physical properties [24, 31, 32]. Due to its ability to increase the production of photocatalytic reactions, this technology is particularly helpful in the field of semiconductor research and has attracted a lot of interest. The doping process can enhance the photocatalytic activity base on the increase of light absorption with the narrow band gap, and alter the desirable element for electronic and optical properties. Among numerous elemental doping strategies, oxygen (O) and phosphorus (P) doping have garnered a great deal of attention. Oxygen doping can significantly increase the quantity of O-containing functional groups on the surface and alter the N in the g-C_3N_4 framework, which improves the charge transfer and slow down the recombination rate

of the electron-hole pairs [33, 34]. Otherwise, phosphorus doping is demonstrated for great photocatalytic activity due to introducing additional energy levels into the band structure [23, 35]. Despite these advanced properties, the doping method has several drawbacks, such as difficulties in regulating the concentration of the dopant and the potential to introduce unintended contaminants into the substance. Moreover, the O and P co-doped are not thoroughly discussed thus far in the photocatalytic reaction. This led to our belief in the need for studying this knowledge.

1.4 Photodegradation of tetracycline hydrochloride antibiotic

Antibiotics are considered one of the greatest medical discoveries of the 20th century, which are used to prevent and treat bacterial infections. Nonetheless, the overuse of antibiotics in daily life and livestock farming has led to antimicrobial resistance. In the natural habitat, the antibiotic residues from domestic sewage and breeding are discharged into the soil and aquatic environment, which increases the concentration of toxins, causing a threat to its ecosystem function. Around the world, in 2019, more than 1 million people were killed and almost 5 million deaths were correlated with antibiotic residues [36]. As a result of its detrimental effects on human health and livestock security, antibiotic residues in the environment have gained widespread attention.

Tetracycline hydrochloride (TC) is one of the most common pharmaceutical residues belonging to a broad-spectrum antibiotic with a stable four-ring structure (Figure 1), which prevents bacteria from synthesizing proteins by disrupting the bindings of aminoacyl-tRNA to the ribosome [37]. Therefore, a variety of methods have been developed to remove TC from an aqueous environment, including membrane separation, biodegradation, adsorption, Fenton oxidation, and photocatalyst degradation [38-40]. Among them, the photodegradation process is considered a superior strategy for the elimination of TC based on its low cost, sustainable technology, and high removal efficiency [19, 41, 42].

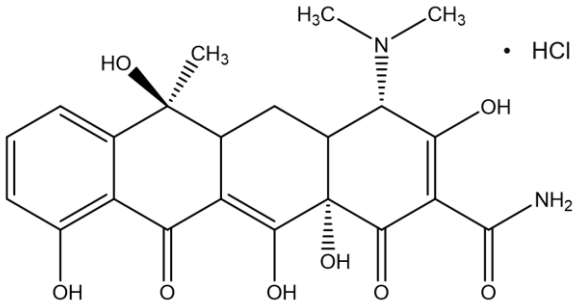

Figure 1. Tetracycline Hydrochloride structure.

Two steps can be implemented to explain the photodegradation mechanism of TC utilizing g-C_3N_4 in an aqueous solution: Initial electrostatic interactions and van der Waals forces between the adsorbate and the photocatalyst surface enable the pollutant to be absorbed on the g-C_3N_4 surface. There is a slow reduction in the concentration of TC in the aqueous solution at this point, and this amount of TC is of no significance. After the absorption phase, the light source is turned on and starts the light phase. Under visible light irradiation, the electron-hole pairs separate, generating the photoelectrons transfer to the g-C_3N_4 surface to facilitate the formation of reactive species, such as hydroxyl radicals and superoxide radicals. These radicals, especially the superoxide radical known as the main break down TC into degradation products, which are less harmful molecules or CO_2 and H_2O. Besides that, the holes in g-C_3N_4 also can directly oxidate TC at another pathway. As a result, it is necessary to use photocatalysts with the appropriate range of bandgaps to facilitate the photodegradation of TC, and g-C_3N_4 is one of the most suitable catalysts.

1.5 Water splitting photocatalyst for H_2 evolution reaction

In recent decades, the consumption of energy and the requirements for energy has increased rapidly as a result of population growth, industrialization, and technological advancements. Energy consumption is primarily derived from fossil fuels such as coal, oil, and natural gas, which account for 66% of total energy consumption (Figure 2). The availability of these resources is currently declining drastically, and they will be difficult to replenish soon. Further, fossil fuels are regarded as the main source of CO_2 emissions that contribute to global warming [43].

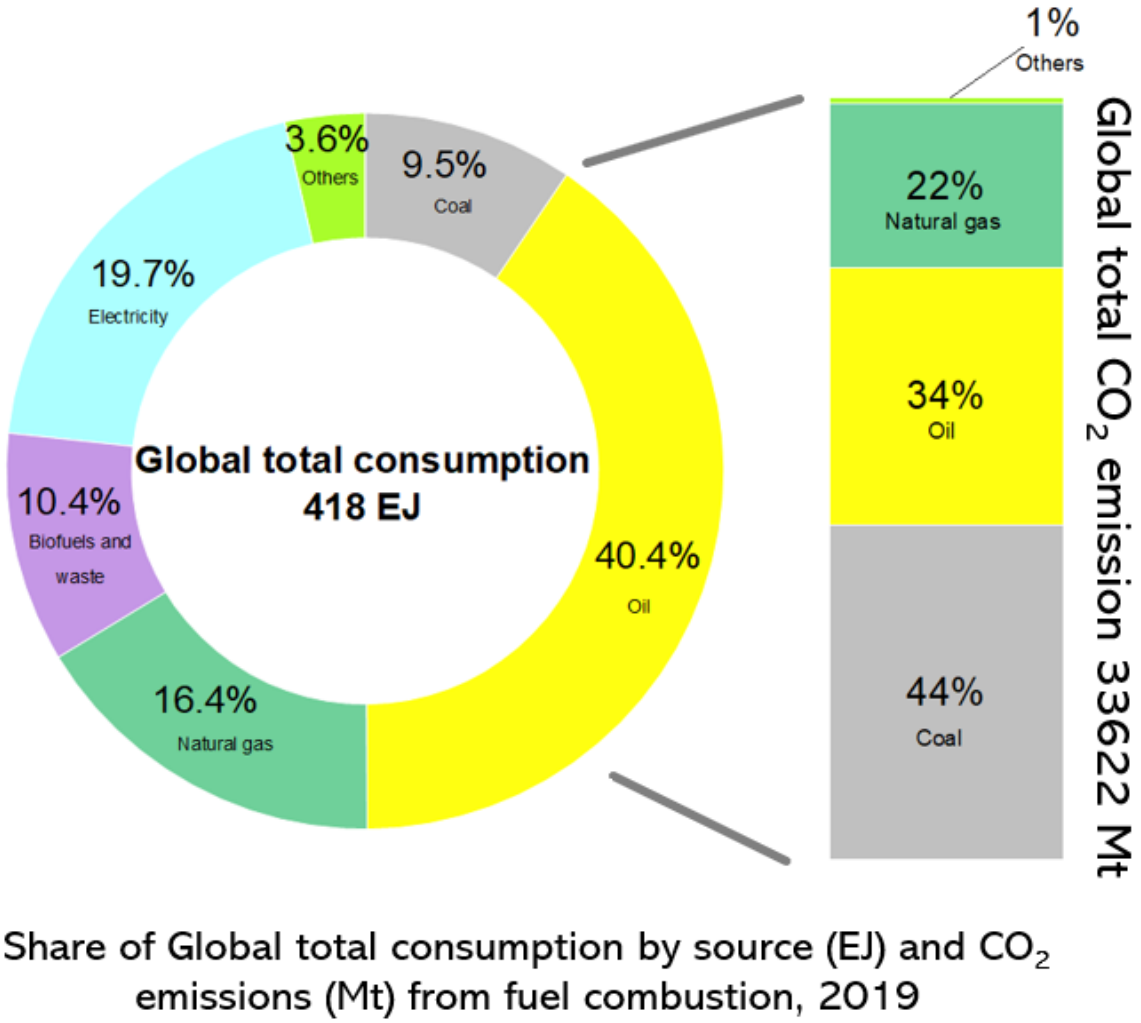

Figure 2. The Global total consumption by source and CO_2 emissions from fuel combustion in 2019 [43]

Several strategies have been implemented by the governments to reduce dependence on fossil fuels, such as reducing energy consumption and improving the efficiency of private and industrial buildings; particularly the use of renewable energy sources [44]. As a renewable energy resource, hydrogen from photocatalytic water-splitting based on semiconductors has the potential to meet the green energy mandate of no CO_2 emissions as sunlight and water are clean, abundant, and renewable sources. In addition, Pt is one of the most popular and important elements in hydrogen evolution reactions due to its active site and stability. Its active site involves the adsorption and

dissociation of hydrogen atoms for generating H_2 [45]. The hydrogen evolution reaction mechanism can be described in three-step: i) Light absorption to generate electron-hole pairs, ii) The charge transfer and separation of electrons, iii) Surface redox reaction for hydrogen evolution reaction with Volmer reaction ($H_2O + e^- \rightarrow H_{ads} + OH^-$) and Tafel reaction ($H_{ads} + H_{ads} \rightarrow H_2$). Under light irradiation, the electrons from the VB of the g-C_3N_4 can be excited into the CB and leave the holes at the VB. Owing to the Fermi level difference between g-C_3N_4 and Pt, the Schottky barrier was formed and the photogenerated electrons are easily shifted from the g-C_3N_4 to the Pt via this energy barrier. Subsequently, the electrons are transferred to the surface of Pt and enrolled in the Volmer step, which generates absorbed hydrogen atoms. Finally, in the Tafel reaction, molecular hydrogen formation by the connection of two adsorbed hydrogen atoms [46].

1.6 Research objectives

Through surface modification of g-C_3N_4 using a couple of facile synthesis processes, this thesis aims to enhance the photocatalytic performance and properties of this material. Hence, the studies are organized around two primary goals.

For the first study, the extension of the melem unit and further growth of the extended melem unit during the hydrothermal treatment and the effect on the photocatalytic behaviors will be carefully evaluated for the photodegradation of TC in an aqueous solution under visible light irradiation. Various hydrothermal treatment times for modifying the CN will be chosen at different periods. XRD, FTIR, TEM, BET, XPS, UV-Vis DRS, EIS, PL, and TRPL will be conducted on each sample to analyze their characteristics. Finally, TC removal performance will be performed to assess the effect on the photodegradation efficiency of TC.

The second research involves investigating the electronic and physicochemical effect of the Oxygen and Phosphorus co-doped over CN_U by hydrogen evolution reaction. Furthermore, the interface interaction between O-groups, Phosphorus, and Pt valence state formation will be examined. The calcination technique will be used to synthesize co-doped photocatalysts in a one-step synthesis. In addition, the properties of the prepared photocatalysts will be characterized by various techniques.

Chapter 2. MATERIALS AND METHOD

2.1 Catalyst preparation

Pristine g-C_3N_4 was synthesized by a thermal polycondensation method. The precursor, thiourea (30 g) (CH_4N_2S, ≥99%, supplied by Sigma-Aldrich Korea, South Korea), was placed in a crucible covered with aluminum foil and heated to 550 ◦C for 4 h (ramping rate = 5 ◦C/min) in a muffle furnace. The as-synthesized bulk g-C_3N_4 sample was named CN. One gram of CN powder was dissolved in 100 mL of DI water and then sonicated for 2 h at room temperature. The 150 mL Teflon™ autoclave containing the CN-180-x samples (x = 3, 6, or 9 h where x was the hydrothermal period) was heated in an oven to 180 ◦C (ramping rate = 5 ◦C/min). In comparison with the CN-180-6, the CN-200-6 was synthesized in 6 h at 200 ◦C. The resulting materials were repeatedly rinsed with DI water after cooling to room temperature before being freeze-dried for the photocatalytic activity test and further characterization. The schematic procedure for CN_T and catalyst synthesis was illustrated in Figure 3.

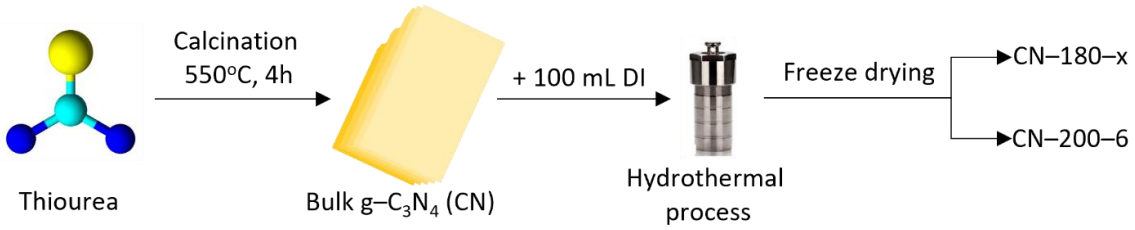

Figure 3. The synthesis of CN, CN-180-x, and CN-200-6.

The oxygen and phosphorus co-doped g-C_3N_4 (O_yPCN_U) samples were synthesized via one-pot polymerization treatment of urea, hypophosphorous acid, and a certain amount of ammonium persulfate as a dynamic gas template and O precursor. Firstly, the urea bulk (CN_U) was calcined at 550°C for 2h in a crucible covered with aluminum foil with ramping rate = 5 ◦C/min in a muffle furnace. The preparation process is as follows: 10g of urea and y(g) of ammonium persulfate were ground and mixed well together, where y = 1.5, 2.5, and 3.5. After transferring the mixer to a ceramic crucible (50mL), a 5mL solution of 1 wt.% P was added and stirred to form a homogeneous slurry. The final mixer was calcined with the same procedures in CN_U preparation. For the

hydrogen evolution reaction test, a magnetic stirrer was used to dissolve the O_yPCN_UPt samples in 1000 mL of DI water for 60 min. The $H_2PtCl_6 \cdot 6H_2O$ amount added to the mixture was calculated to set the initial content of Pt at 3 wt.%. Pt on O_yPCN_U was processed with hydrogen reduction for 60 min under a 30 rpm H_2 flow rate at 60 °C. The precipitates were collected and dried under 70°C oven temperature for additional characterization in the final step. The materials were CN_UPt, $O_{1.5}PCN_UPt$, $O_{2.5}PCN_UPt$, and $O_{3.5}PCN_UPt$, according to their O_yPCN_U precursors. The schematic of O_yPCN_U and O_yPCN_UPt synthesis is illustrated in Figure 4.

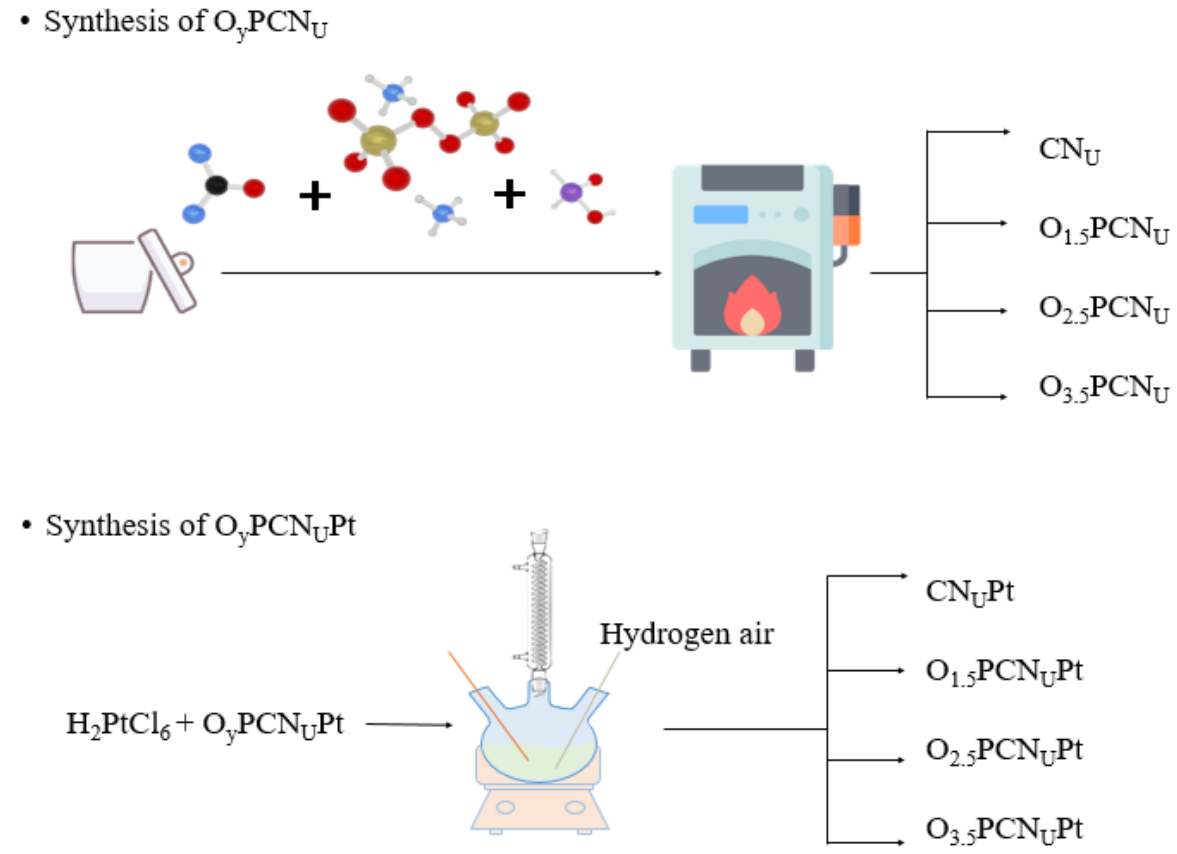

Figure 4. The synthesis of $OyPCN_UPt$ catalysts.

2.2 Characterization

A QUADRASORB™ SI surface area instrument (Quantachrome Instruments, Boynton Beach, FL, USA) and N_2 adsorption-desorption isotherms were applied to measure the Brunauer–Emmett–Teller (BET) specific surface areas. The morphologic changes of the CN-180-x and CN-200-6 were determined by transmission electron microscopy (TEM) Tecnai G2 F20 X-TWIN (FEI, Austin, TX, USA). The Pt element composition of O_yPCN_UPt samples was validated using an inductively coupled plasma–optical emission spectrometer (ICP-OES) (700-ES; Varian Australia Pty. Ltd., Mulgrave, Australia). The morphologies of the O_yPCN_UPt samples were investigated using Scanning transmission electron microscopy (STEM) (JEM-ARM300F, JEOL, Japan) and Field-emission scanning electron microscopy (FE-SEM) (Quanta 200 FEG, FEI Corp., Hillsboro, OR, USA). A Cu K X-ray source with a wavelength of 1.5415 (scan rate of 2◦ (2θ)/min) was used to study the X-ray diffraction (XRD) patterns of the photocatalytic samples using a D/MAZX 2500 V/PC high-power diffractometer from Rigaku (Tokyo, Japan). A Fourier transform infrared (FTIR) transmittance spectrometer (Nicolet™ 380 spectrometer, Nicolet™ iS5 with an iD1 transmission accessory by Thermo Scientific™, Waltham, MA, USA) was employed to determine the functional groups of the produced photocatalysts. X-ray photoelectron spectroscopy (XPS) was carried out using Thermo Scientific's K-Alpha system.

A UV–Vis diffuse reflectance spectrometer (UV-DRS) (SPECORD® 210 Plus spectroscope; Analytik Jena, Germany) examined the optical characteristics of the photocatalysts. The electrochemical impedance spectroscopy (EIS) data was conducted on an impedance analyzer (VSP series; Bio-Logic Science Instruments, Seyssinet-Pariset, France). A fine powder mixture containing 20 mg catalyst sample and 2 mg of active carbon was added into 100 µL isopropanol 99.7% and 30 µL Nafion 5 wt.% (both from Sigma-Aldrich Korea, Gyeonggi, South Korea). The electrolyte for the three-electrode electrochemical cell consisted of 10 mL of a 1 M NaOH solution. While a RE-1BP (Ag/AgCl) electrode was the reference electrode, the platinum wire was the counter electrode, and the working electrode was a 6 mm standard glassy carbon electrode. To measure the EIS, 10 µL of the obtained mixture was carefully coated onto the glassy carbon electrode. Then, setting a frequency range of 0.01 Hz to 100 kHz with a 10 mV amplitude and a

direct current potential of +0.8 VSCE was utilized. For additional verification of the charge carrier recombination rate, time-resolved photoluminescence (PL) spectra were analyzed by an FS5 spectrofluorometer (Edinburgh Instruments Ltd., Livingston, UK) under 400 nm laser excitation and the emission decay was fitted with tri-exponential functions.

2.3 Photocatalytic activity

2. 3. 1 Photodegradation test

The photocatalytic activities were conducted by an Oriel's Sol1A™ Class ABB system with a 140 W xenon lamp and UV cut-off filter (λ > 420 nm) as the light source. In a typical photodegradation, 10 mg of as-prepared samples were suspended in 50 mL of 20 ppm TC. Before the photocatalytic reaction, the suspension was stirred for 60 min in the dark phase to achieve adsorption–desorption equilibrium and then irradiated for 2.5 h at the ambient temperature. At 30 min intervals, 3 mL of the solution was filtered through a polytetrafluoroethylene membrane filter (Whatman GmbH, Dassel, Germany) and analyzed by absorbance at λ_{max} = 357 nm as a function of the amount of radiation it received, which was measured using a SPECORD 210 Plus spectroscope. The pseudo-first-order kinetic model was followed by Equation 1:

$$\ln\frac{C}{C_0} = -kt \qquad (1)$$

where C_0 (mg/L) was the initial concentration of TC before irradiation, C was the actual TC concentration at time t, and k was the kinetic rate constant (min^{-1}) [47, 48]. In addition, to confirm the reusability of the as-prepared samples, a 4-cycle experiment was carried out for 50 min for each run under the same reaction conditions.

The role of the reactive species in the removal of TC over the CN-180-6 samples was determined by some specific scavengers. Specifically, 5 mM Teoa triethanolamine (TEOA) (h^+ quenching agent), 5 mM isopropyl alcohol (IPA) (•OH quenching agent), and 5 mM p-benzoquinone (BQ) ($\bullet O_2^-$ quenching agent) were dropped into the solution for the quenching experiments.

2. 3. 2 H_2 evolution reaction test

For the photocatalytic H_2 evolution experiments, a solar simulation system with a light source consisting of an LED lamp with a light intensity set to 100 $mW.cm^{-2}$ was used. Each photocatalyst (30 mg) was then dissolved for 30 min with high-purity Argon purging in the dark in 100 mL of DI water. As a hole scavenger, 10 mL of triethanolamine (TEOA) was incorporated into the solution. Argon was used to purge the reactor system before starting H_2 evolution tests. An online gas chromatograph with an installed thermal conductivity detector was utilized to examine the gas products. The same setup in 5 h cycles was used for the photocatalyst stability tests. At the beginning of each cycle, an extra amount of TEOA (10 mL) was added to the solution, and Argon was again used to purge the reactor system.

Chapter 3. RESULTS AND DISCUSSION

3.1 The growth of extended melem units

3. 1. 1 Physicochemical properties

The N_2 adsorption–desorption isotherms of the as-prepared photocatalysts were depicted in Figure 5. All the samples obviously exposed type IV isotherms with a hysteresis curve of the type H3 pattern, confirming the mesoporous characteristic of the catalysts. Otherwise, the specific BET surface area (S_{BET}), pore volume (V), and average pore diameter (L) of the samples are represented in Table 1. During the hydrothermal treatment, the S_{BET} and V values for the CN-180-x and CN-200-6 samples had a volcano pattern with a maximum at CN-180-6. The highest values were 75.0 $m^2\ g^{-1}$ of S_{BET} and 0.60 $cm^3\ g^{-1}$ of V, respectively, which were almost 3 times higher than those for CN (28.5 $m^2\ g^{-1}$ and 0.20 $cm^3\ g^{-1}$). The high specific surface area can enhance the light-harvesting and improve the photodegradation performance of the photocatalyst. However, the CN-180-9 and CN-200-6 showed lower S_{BET} and V values due to a longer hydrolysis time and a higher hydrothermal temperature. This could be related to the strong hydrolysis/oxidation degree and the attachment of O-containing groups over g-C_3N_4, which will be clarified later in the TEM images and XPS data.

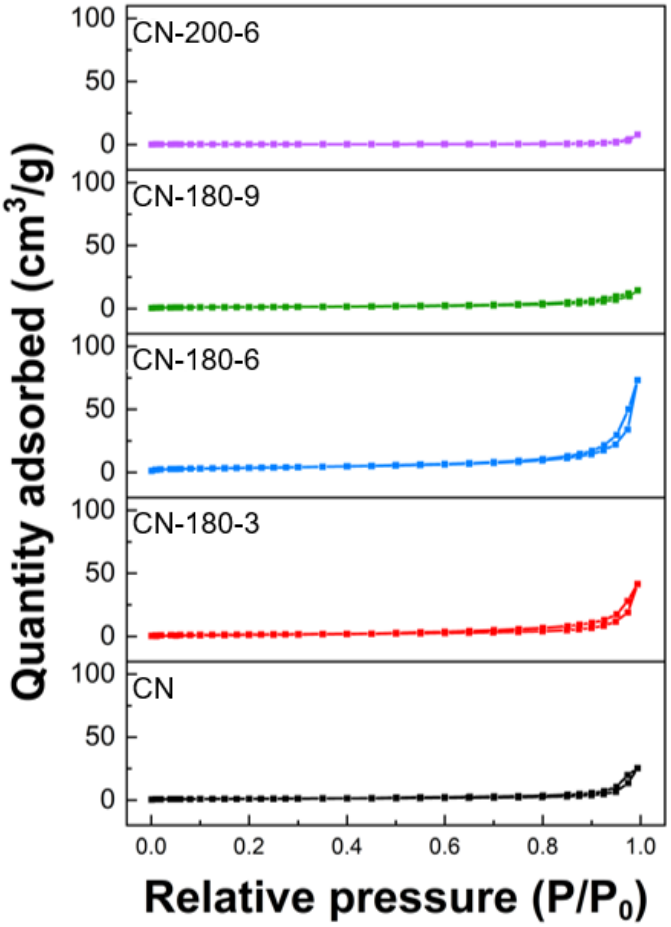

Figure 5. N_2 adsorption/desorption isotherms of as-prepared photocatalysts.

Table 1. Specific surface area, pore volume, and average pore size of photocatalysts were determined via N_2 adsorption-desorption isotherm measurements.

Samples	S_{BET} (m^2/g)	V (cm^3/g)	L (nm)
CN	28.516	0.201	0.030
CN-180-3	58.950	0.347	0.012
CN-180-6	75.000	0.603	0.005
CN-180-9	27.534	0.113	0.002
CN-200-6	5.032	0.065	0.002

The morphological structures of the CN-180-x and CN-200-6 samples were examined by TEM images. As displayed in Figure 6, all of the as-prepared samples exhibited a typical two-dimensional sheet-like structure. In comparison to the clean surface of the CN-180-3 (Figure 6a), the CN-180-9 and CN-200-6 showed the obvious pothole structure on the surface of g-C_3N_4 due to the longer hydrothermal time and the higher temperature, resulting from further hydrolysis on the g-C_3N_4 surface structure (Figure 6c,d). However, the CN-180-6 displayed less pothole structure but significant unevenly porous cracks on the surface at high magnification, implying the highest specific surface area for CN-180-6.

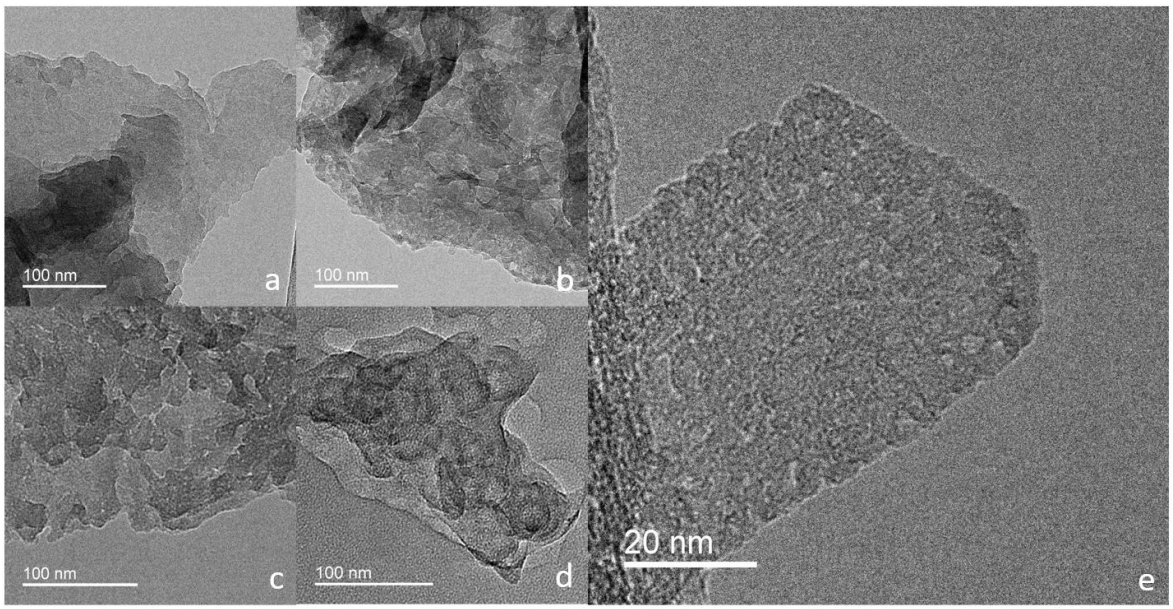

Figure 6. TEM images of CN-180-3 (a), CN-180-6 (b,e), CN-180-9 (c), and CN-200-6 (d).

The crystal structures of all synthesized photocatalysts were analyzed by the XRD measurement (Figure 7A). For pristine CN, two characteristic peaks appearing at 12.6 and 27.7° could be ascribed to the (100) and (002) crystal planes of the graphite-like structure of CN, respectively (JCPDS 87-1526) [49]. The significant peak centered at 27.7° was related to the interplanar staking in the g-C_3N_4 and the minor diffraction peak at 12.6° corresponded to the in-plane tri-s-triazine unit in the g-C_3N_4 [50-52]. After the hydrothermal process, the typical XRD diffraction peak at 27.7° for as-synthesized samples remained not notably different, maintaining the

strong crystallinity. However, with increasing hydrothermal time and temperature, a new peak arising around 10.6◦ was increased along with the gradual decrease of the peak at 12.6°. First, the peak shift from 12.6 to 10.6° corresponded to the extension of the in-plane staking structure (the melem unit) from 0.68 nm to 0.83 nm [53]. Second, the sharp peak at 10.6° could be interpreted as the growth of the extended melem unit during the hydrothermal treatment. Therefore, the extension of the melem unit started at CN-180-6, and the extended melem unit was continuously grown by the further hydrolysis process.

Meanwhile, the chemical structure of the as-prepared samples was monitored by FTIR spectroscopy (Figure 7B). The intense peak at 810 cm^{-1} represented the characteristic vibration mode of the triazine unit. The absorption bands located at 1200–1600 cm^{-1} were assigned to the typical stretching mode of the C-N aromatic structure. Broad bands at 3000–3600 cm^{-1} were the result of the uncondensed terminal amino groups or hydroxyl groups [41, 54]. The main peaks of the CN-180-x and CN-200-6 samples were consistent with the pristine g-C_3N_4, confirming that the main chemical structure of graphitic carbon nitride was maintained even after the hydrothermal treatment for a long time and at high temperatures.

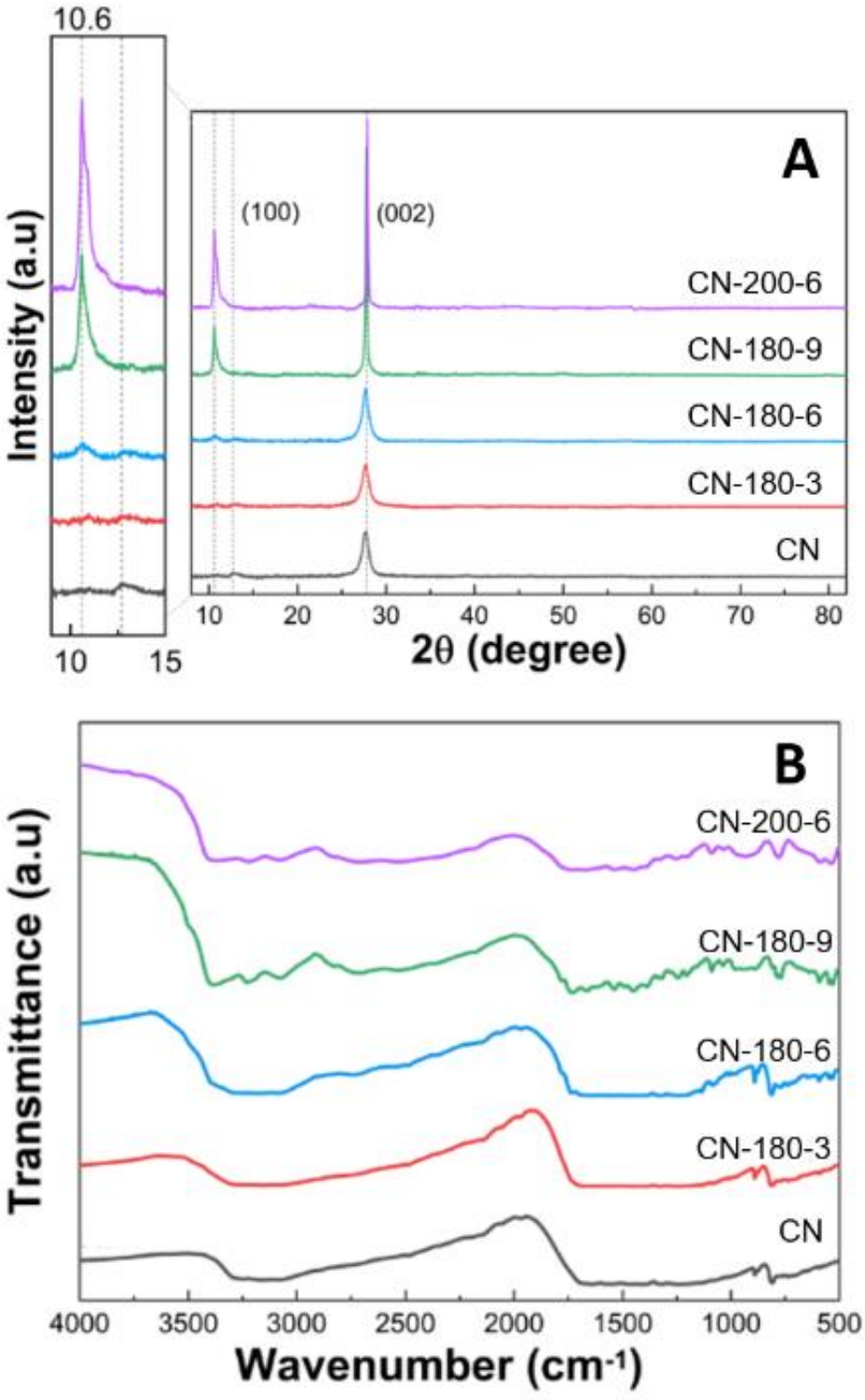

Figure 7. (A) XRD patterns and (B) FT-IR spectra of CN-180-x and CN-200-6 samples.

Additionally, the XPS measurement was employed to further probe the chemical bonding states of all the photocatalysts. In Figure 8, the XPS data of C 1s, N 1s, and O 1s for the CN-180-x and CN-200-6 samples are shown. In the C 1s spectra, the peak centered at 287.8 eV was related to the sp^2 -bonded carbon (N–C=N), and the peak at 284.5 eV corresponded to C-C bonds [55, 56]. During the hydrothermal treatment, the deconvolution of C 1s displayed other peaks centered at 289.0 eV and 286.3 eV, which were assigned to the –COOH species and the −NHx groups, respectively [57-60]. The N 1s spectra of the as-prepared samples could be fitted into three characteristic peaks centered at 398.0 eV, 398.7 eV, and 400.6 eV, relating to the pyridine N (C-N=C), the bridging N atoms in $N-(C)^3$, and the amino groups with H, respectively [61, 62]. Meanwhile, the O 1s XPS data of the CN-180-x and CN-200-6 samples showed three prominent peaks at 530.6 eV, 531.5 eV, and 533.0 eV, which were attributed to −COOH, −OH, and the C=O species, respectively [63-65]. After the hydrothermal process, the intensities of the peaks at 530.6 eV and 533.0 eV were increased, indicating the addition of more O-containing functional groups in the as-synthesized samples, which was also confirmed by the EA results (Table 2). In Table 2, the rapid increase in the atomic ratio of O/N up to CN-180-9 implied the introduction of more O-functional groups onto the $g\text{-}C_3N_4$ surface. Even though CN-180-9 obtained the highest ratio of O/N compared to all the photocatalysts, its morphological structure displayed fewer defects than the CN-180-6, which was confirmed in the TEM images. These resulted in a lower S_{BET} value for CN-180-9 than that for CN-180-6 (Table 2).

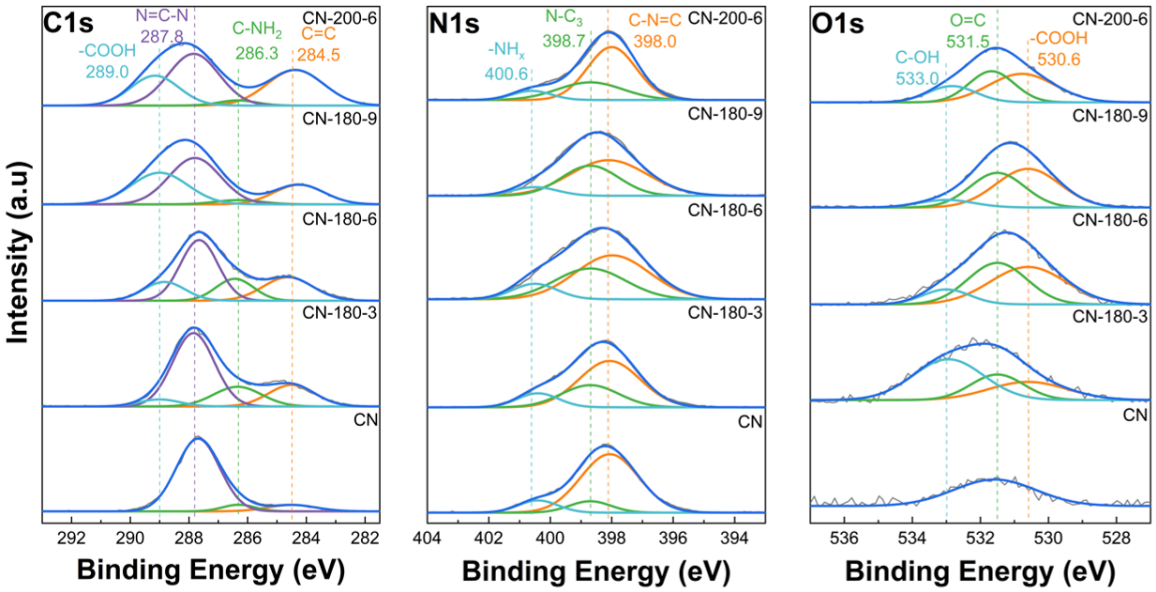

Figure 8. XPS data of C 1s, N 1s, and O 1s for all the photocatalysts.

Table 2. C/N and O/N atomic ratios of all prepared samples were obtained from elemental analysis.

Sample	Element Analysis				
	Atom (wt.%)			Atomic Ratio	
	C	N	O	C/N	O/N
CN	33.8	60.3	4.5	0.65	0.07
CN-180-3	32.3	58.2	7.6	0.65	0.11
CN-180-6	29.7	53.3	13.5	0.65	0.22
CN-180-9	28.5	50.4	17.6	0.66	0.31
CN-200-6	31.5	56.1	10.3	0.66	0.16

3. 1. 2 Optical properties of modified g-C_3N_4

The optical absorption properties of the as-synthesized samples were investigated by the UV–Vis diffuse reflectance spectra (UV-DRS). As shown in Figure 9A, the absorption edge of CN, CN-180-x, and CN-200-6 were in the range of 300–520 nm, from the UV to the visible light region [66]. In comparison to all prepared samples, CN-180-6 displayed a red shift and broad absorption throughout the visible spectrum, corresponding to the light-harvesting improvement for the photocatalytic reaction [67]. Additionally, the energy band edges (E_g) of the catalysts were estimated by the Tauc plot method and displayed in Figure 9B. The E_g values for CN, CN-180-3, CN-180-6, CN-180-9, and CN-200-6 were estimated at 2.72, 3.09, 2.83, 3.21, and 3.11 eV, respectively, which slightly enlarged with the integration of the O groups during the hydrothermal treatment. Moreover, the valence bands (E_{VB}) and the conducting band (E_{CB}) of the CN-180-x and CN-200-6 samples were conducted according to the empirical equation as follows [68]:

$$E_{VB} = \chi - E^e + 0.5E_g \quad (2)$$

$$E_{VB} = E_{CB} + E_g \quad (3)$$

where χ possessed the absolute electronegativity of the semiconductor (about 4.73 eV); E e was the energy of free electrons (about 4.5 eV). Hence, the E_{VB} values for CN-180-3, CN-180-6, CN-180-9, and CN-200-6 were 1.78, 1.64, 1.84, and 1.79 eV vs. NHE, while the related E_{CB} were −1.32, −1.18, −1.37, and −1.33 eV vs. NHE, respectively (shown in Figure 10).

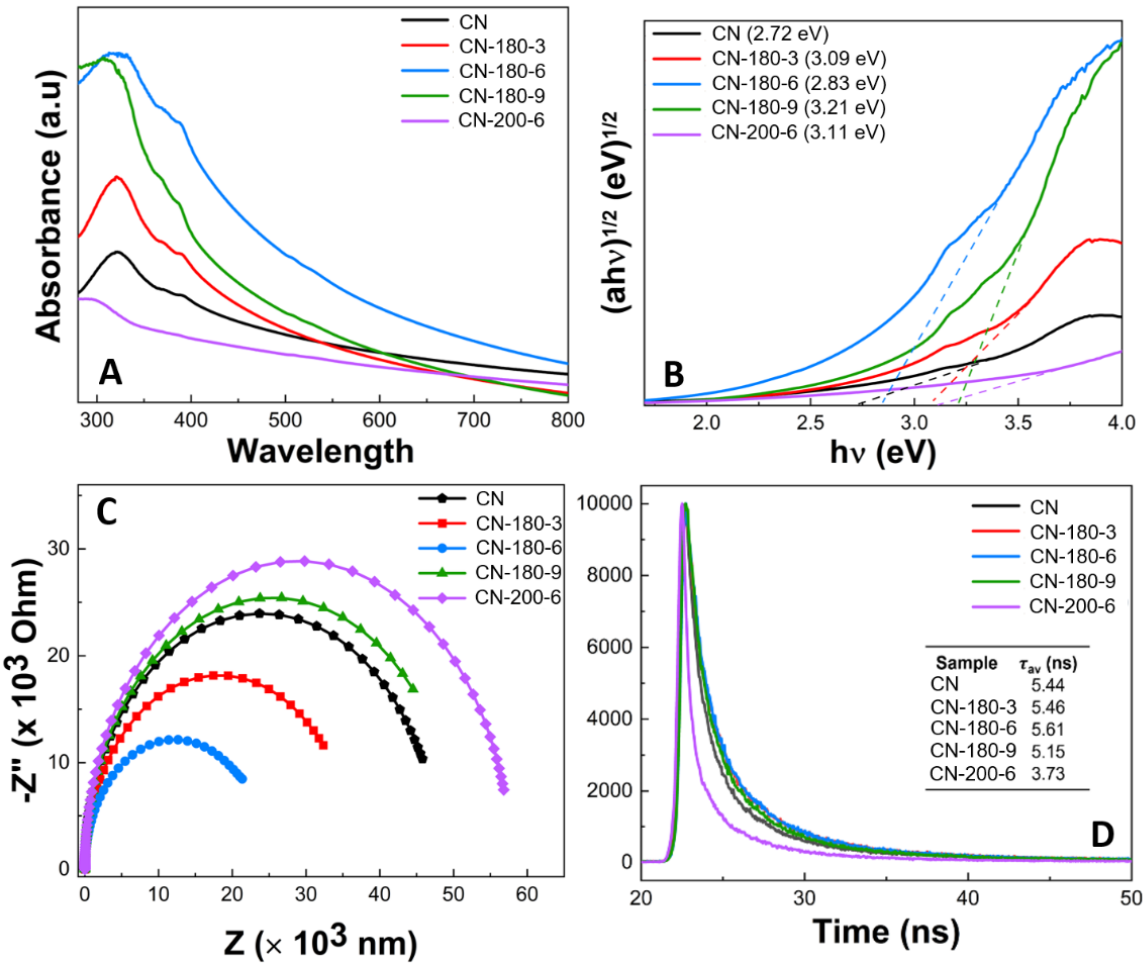

Figure 9. (A) UV–Vis DRS absorption spectra, (B) Tauc plots for the band gap, (C) the EIS Nyquist plots, and (D) time-resolved fluorescence decay spectra in the ns time scale with excitation 400 nm (inset table: the calculated average fluorescence lifetime (τ_{av})) of as-synthesized CN-180-x and CN-200-6 samples.

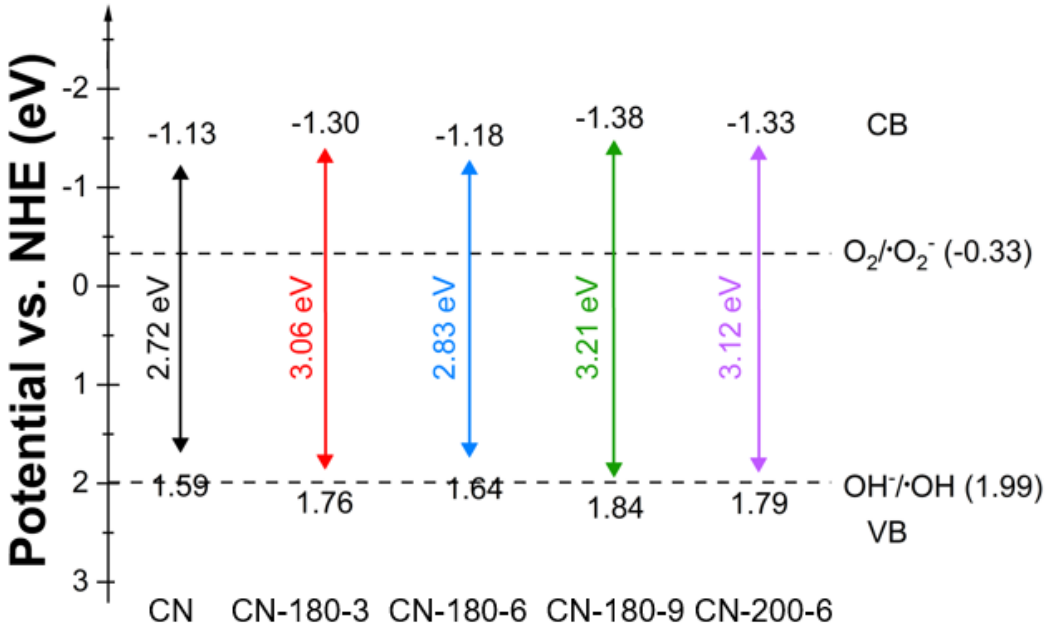

Figure 10. Band diagrams of the CN-180-x and CN-200-x photocatalysts.

Electrochemical impedance spectroscopy (EIS) was an effective analysis to assess the charge transfer efficiency of the photocatalysts. As depicted in Figure 9C, the diameter of the arc radius for the as-prepared samples gradually declined from CN, CN-180-3, and CN-180-6. The EIS Nyquist plot of CN-180-6 revealed the smallest semicircle arc radius, suggesting the highest separation and transfer efficiency of the electron–hole pairs [69, 70]. Interestingly, the CN-180-9 and CN-200-6 samples exhibited higher O-containing functional groups than the pristine g-C_3N_4; nevertheless, the arc radius of CN-180-9 and CN-200-6 were larger than that of the bulk, which demonstrated that the growth of the extended melem unit during the hydrothermal process could directly contribute to increasing the g-C_3N_4 surface resistance, resulting in the retardation in the transfer of charge carriers. To confirm the photogenerated electron transfer dynamics, the time-resolved PL decay spectra were investigated and fitted by a tri-exponential function (shown in Figure 9D). The average lifetime (τ) of the charge carrier of the as-prepared samples was obtained by the following Equation (4):

$$\tau = \frac{A_1\tau_1 + A_2\tau_2 + A_3\tau_3}{A_1 + A_2 + A_3} \quad (4)$$

where A_1, A_2, and A_3 are the corresponding amplitude, and τ_1, τ_2, and τ_3 are the lifetime [71]. The CN-180-6 displayed slower exponential decay kinetics and its τ value was 5.61 ns which was much higher than that for CN (5.44 ns), CN-180-3 (5.46 ns), CN-180-9 (5.15 ns), and CN-200-6 (3.73 ns). The results implied that the formation of the O-containing melem unit during the hydrolysis/oxidation reaction initially greatly prolonged the lifetime of the photocarrier, enhancing their potential for contribution to the photocatalytic reaction [54, 72, 73]. Nevertheless, the longer hydrothermal reaction time and higher temperature negatively reduced the τ value due to the continuous growth of the extended melem unit. It was remarkable that the longer lifetime of the photocatalyst demonstrated the reduction recombination rate of the photogenerated electron, and thus improved the photocatalytic reaction [74]. In addition, the longer TRPL lifetime for CN-180-6 was further well confirmed with its highest charge transfer efficiency (EIS results) and high photodegradation performance.

3. 1. 3 Photodegradation performance

Figure 11A illustrates the photocatalytic activity of the pristine g-C_3N_4, CN-180-x, and CN-200-6 over the degradation of TC. Firstly, the removal of TC was investigated for 60 min under the dark phase to obtain the adsorption–desorption equilibrium. The TC concentration remained unchanged without a light source. After that, the photodegradation tests were conducted under visible light irradiation (λ > 420 nm). In Figure 11B, the TC removal efficiency of the as-prepared samples was exhibited. The photocatalytic activity of the CN-180-x and CN-200-6 was enhanced initially in the order of CN < CN-180-3 < CN-180-6 (67.61, 84.60, and 97.17%, respectively) and declined dramatically for the CN-180-9 > CN-200-6 (57.91 and 23.30%, respectively).

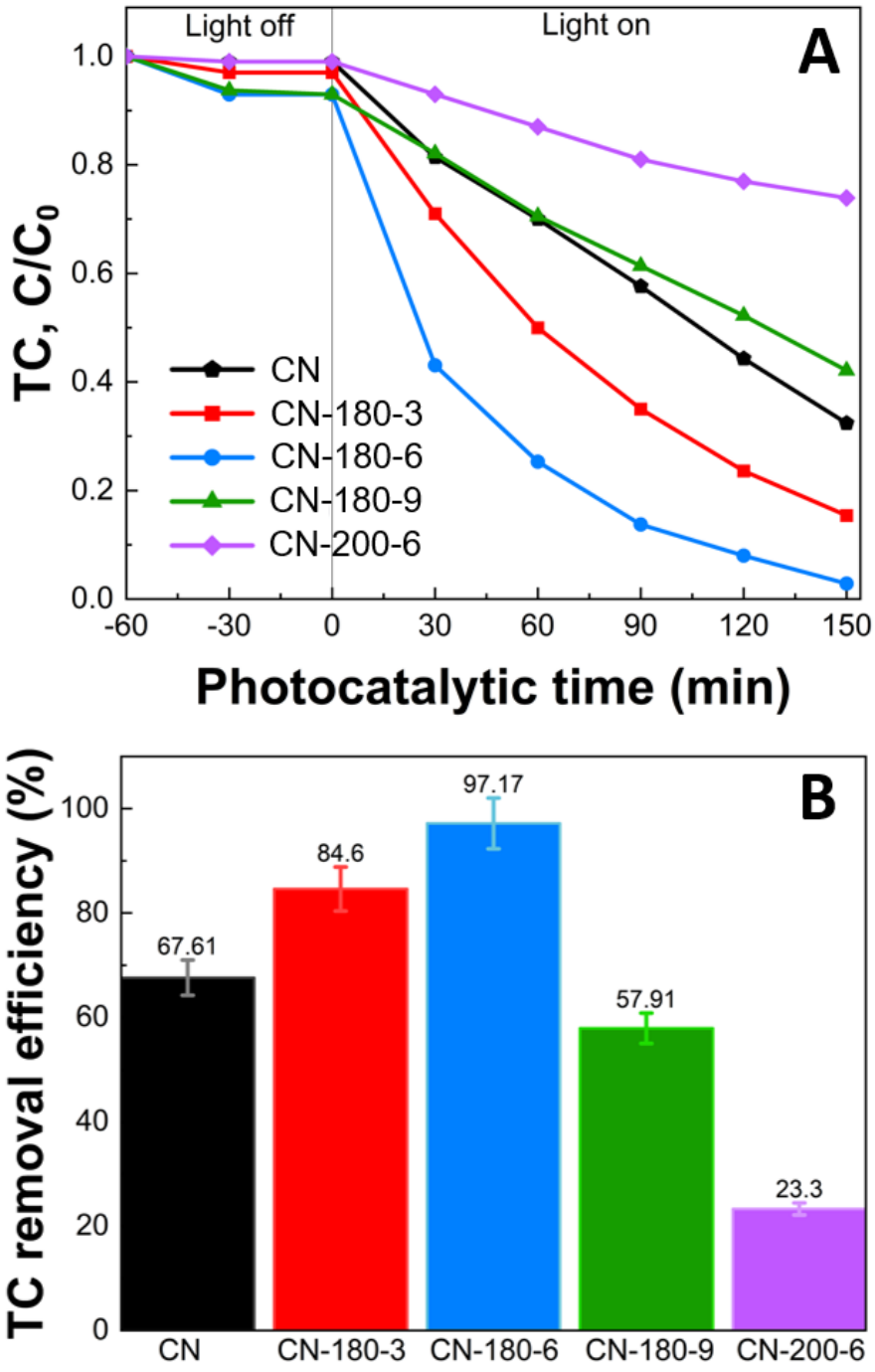

Figure 11. Photodegradation efficiency of TC by CN-180-x and CN-200-6 under visible light irradiation (140W xenon lamp, λ > 420nm) (A) C/C_0 vs. t (Initial condition: 20 mg L^{-1} TC, 0.2 g L^{-1} catalyst, pH = 4.40, 20°C), and (B) TC removal efficiency (%).

The reaction kinetic behaviors of the as-prepared samples were also investigated and demonstrated in Figure 12. According to the pseudo-first-order kinetic equation, all the fitted lines had a high linearity value (R^2 > 0.98) (Figure 12A and Table 3), which showed that the photocatalytic activity can be well modeled by the equation. The reaction rate constant (k) values are displayed in Figure 12B. The k values of TC photodegradation for pristine CN, CN-180-3, CN-180-6, CN-180-9, and CN-200-6 were 0.0066, 0.0118, 0.0236, 0.0058, and 0.0023 min^{-1}, respectively. The k value for degradation of TC over CN-180-6 was about 3.7 times higher than that of CN. It was elucidated that the introduction of O-functional groups onto the melem unit during the hydrothermal process initially increased the reaction rate of the photodegradation, resulting in the highest photocatalytic efficiency of CN-180-6 (97.17%). However, the growth of the extended melem unit despite the abundant addition of O-containing functional groups suppressed the TC photodegradation over CN-180-9 and CN-200-6, which was directly correlated to the charge transfer efficiency. As displayed in Figure 13, the recyclability and stability of the CN-180-6 were evaluated for four continuous cycles (600 min). Under visible light, the photodegradation rate of CN-180-6 was firmly unchanged, demonstrating high activity and stability, making it a promising photocatalyst for TC degradation.

Table 3. Kinetic rate constants (k) and correlation coefficients (r^2) of TC photodegradation.

Sample	$k \times 10^3$ (min^{-1})	r^2
CN	6.6	0.98247
CN-180-3	11.8	0.99719
CN-180-6	23.6	0.98859
CN-180-9	5.8	0.99199
CN-200-6	2.3	0.99224

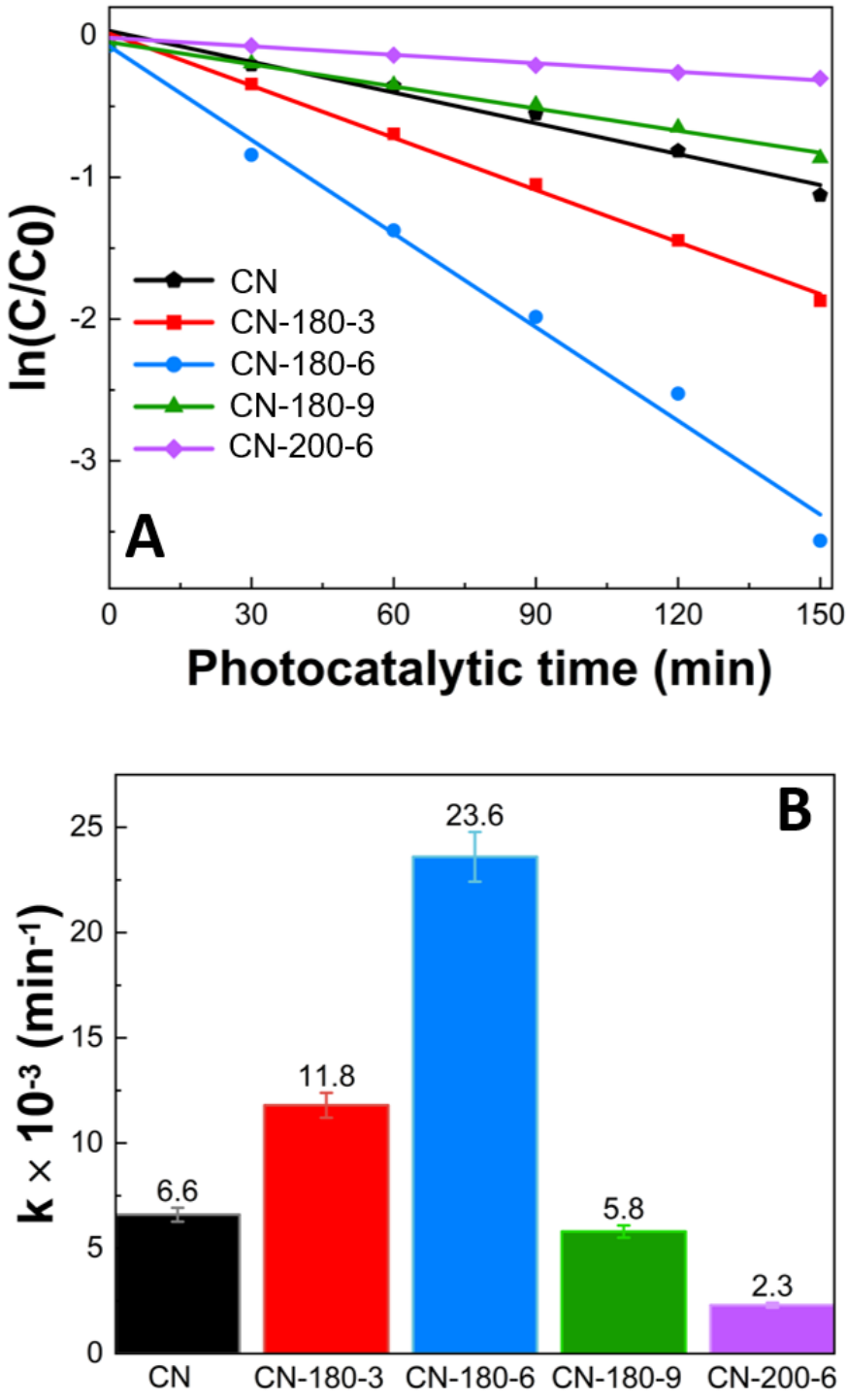

Figure 12. (A) The pseudo-first-order reaction kinetics and (B) rate constants (k) of as-prepared photocatalysts for TC photodegradation.

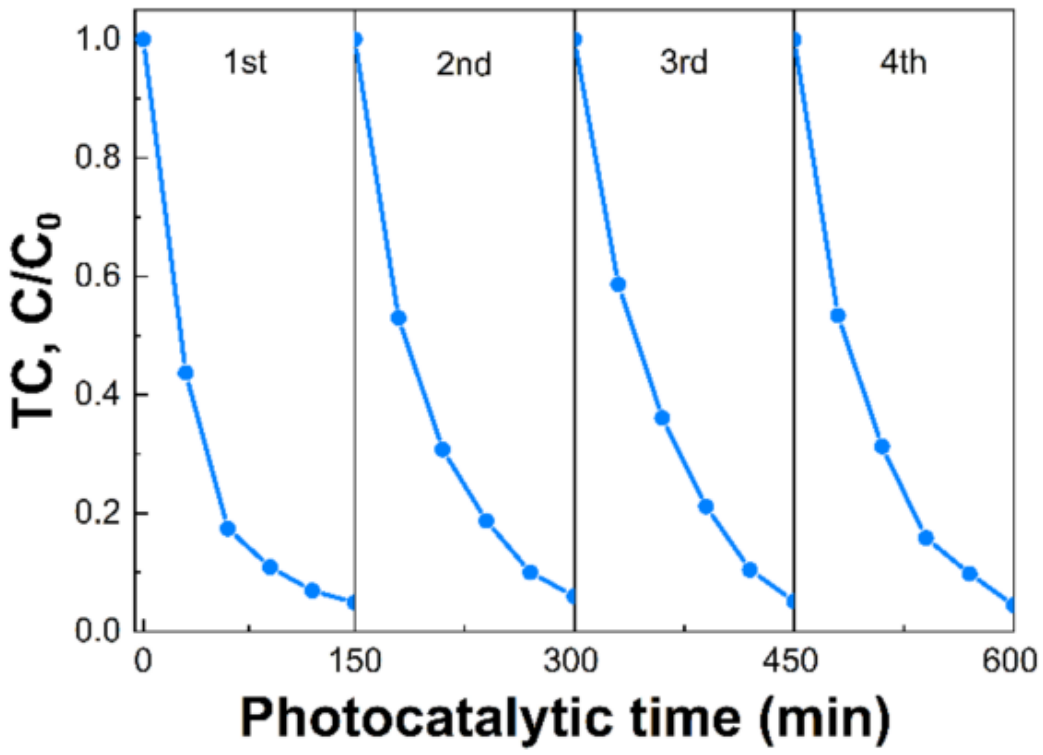

Figure 13. Recycling ability evaluation of CN-180-6.

To investigate the contribution of different reactive species involved in the photocatalytic activity, triethanolamine (TEOA), isopropyl alcohol (IPA), and p-benzoquinone (BQ) were utilized to quench h+, •OH, and $\bullet O_2^-$, respectively [75, 76]. As illustrated in Figure 14, under visible light irradiation, the introduction of IPA and TEOA slightly inhibited the TC removal efficiency from 97.17 to 80.91 and 84.18%, respectively, revealing that the •OH and h+ played a minor role in the TC photodegradation. However, a notable decrease in TC removal (15.86%) was obtained with the addition of BQ, suggesting that $\bullet O_2^-$ was the dominant species in the photocatalytic process. The electron in the CB of CN-180-6 could be excited from the VB and then reduced the O_2 to form the $\bullet O_2^-$ radicals based on the more negative CB potential (−1.18 eV vs. NHE) compared to the standard redox potential of $O_2/\bullet O_2^-$ (−0.33 eV vs. NHE), which was in good agreement with the band structure (Figure 10) [77].

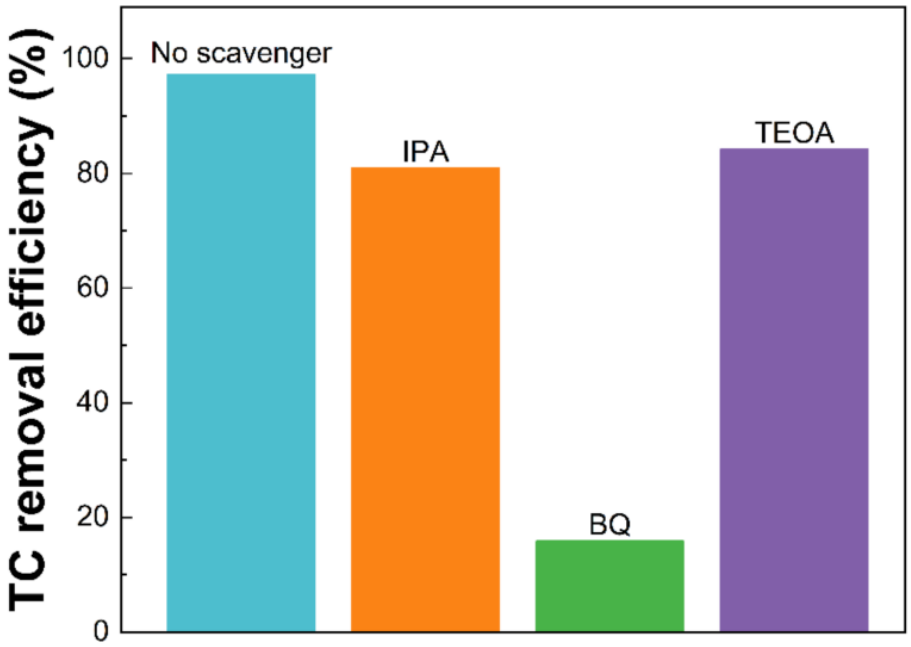

Figure 14. The influence of reactive species on TC removal efficiency (%).

3. 1. 4 Conclusion

In this work, we modified g-C_3N_4 via the hydrothermal treatment under different conditions and applied them for the photodegradation of TC. We found that the hydrothermal treatment induced not only the addition of sufficient O-containing groups into CN but also the formation of extended melem units on g-C_3N_4. The latter inhibited the charge transfer on g-C_3N_4, resulting in a high recombination rate of photogenerated electron–hole pairs. Moreover, the porous crack structure of the extended melem units optimized the specific surface area, which enhanced the visible light absorption and the TC adsorption ability in photocatalytic degradation. The best efficiency of CN-180-6 for the TC degradation under visible light irradiation was achieved at 97.17% because CN-180-6 contained more abundant O-functional groups and less extended melem unit on g-C_3N_4 with the highest specific surface area. Furthermore, from the reactive species test, $\bullet O_2^-$ was proven as a main reactive species involved in the TC degradation.

3.2 The O and P co-doped effect on the H_2 evolution reaction

3. 2. 1 Physicochemical and morphological properties

The Brunauer-Emmett-Teller(BET) technique was used to analyze the specific surface area and pore diameter distributions of the photocatalysts by the N_2 adsorption–desorption isotherms of the as-prepared photocatalysts were shown in Figure 15. The samples exposed type IV isotherms as well as a hysteresis curve with a pattern similar to type H3, which indicates that the catalysts are mesoporous. In addition, the specific BET surface area (S_{BET}), pore volume (V), and average pore diameter (L) of the samples are represented in Table 4. The improved S_{BET} following the other of $CN_UPt < O_{3.5}PCN_UPt < O_{2.5}PCN_UPt < O_{1.5}PCN_UPt$ (40.4 < 59.2 < 69.1 < 70.5 m^2/g). The O and P co-doped significantly enhanced the surface area of the O_yPCN_UPt compared to the CN_UPt sample. The increased O-doping content may have contributed to the reduction of S_{BET} and the decrease in V. The photocatalyst may have a higher surface area, which would enhance its photocatalytic activity.

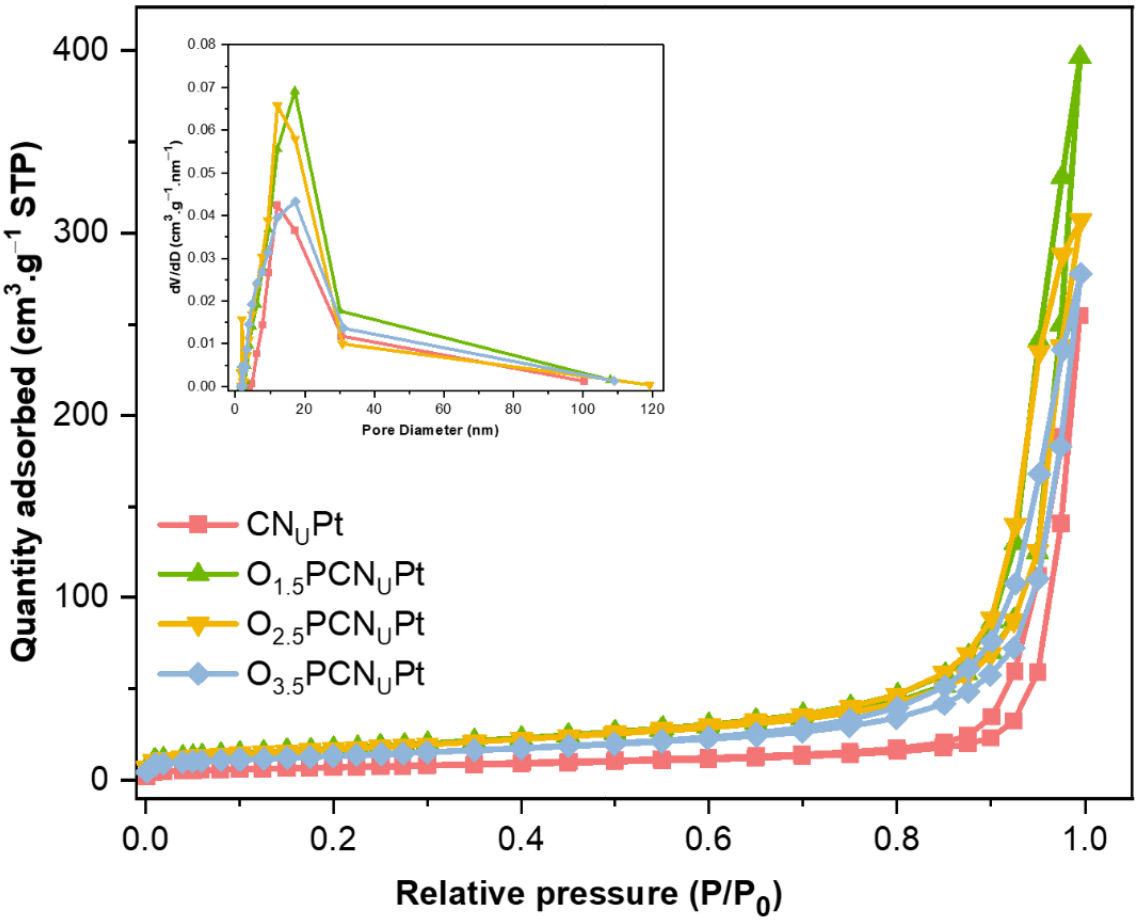

Figure 15. The N_2 adsorption-desorption isotherm and the corresponding pore diameter distribution (insert) of photocatalysts.

Table 4. Specific surface area, pore volume, and average pore diameter of all synthesized samples were determined via N_2 adsorption-desorption isotherm measurements.

Samples	S_{BET} (m^2/g)	V (cm^3/g)	L (nm)
CN_U	40.4	0.39	12.0
$O_{1.5}PCN_UPt$	70.5	0.62	17.0
$O_{2.5}PCN_UPt$	69.1	0.48	12.0
$O_{3.5}PCN_UPt$	59.2	0.48	17.0

The chemical composition of CN_UPt, $O_{1.5}PCN_UPt$, $O_{2.5}PCN_UPt$, and $O_{3.5}PCN_UPt$ was examined using Fourier transform infrared spectroscopy (FTIR) and depicted in the acquired spectra in Figure 16A. The spectra exhibited a strong peak in the 3000-3500 cm^{-1} range, indicating a single-bond interaction with hydrogen (such as hydroxyl groups or NHx groups). The typical aromatic C = N or C-N stretching mode first emerged between 1200-1700 cm^{-1}, while the heptazine cycle shown in the CN structure peaked at 810 cm^{-1} [41, 54]. The results suggested that the main peaks of CN_U were retained following the doping process. Besides, compared to the CN_UPt, two new peaks appeared in the O_yPCN_UPt representing the successful co-doped of O and P in the CN_U structure. The intense peak observed at around 2184 cm^{-1} indicates the vibration mode of cyano groups (– C≡N), and another peak at 1000 cm^{-1} shows the stretching mode of –POx groups [23, 78].

As seen in Figure 16B, XRD measurements were used to examine the crystal structures of the synthesized photocatalysts. According to JCPDS 87-1526, pure CN_U showed two distinctive peaks at 12.6 and 27.7°, which, respectively, correspond to the (100) and (002) crystal planes of the structure of CN_U. The small peak at 12.6° matched the in-plane tri-s-triazine unit in the g-C_3N_4 and the peak centered at 27.7° to the interplanar stacking in the g-C_3N_4 [50-52]. After the doping process, the typical XRD diffraction peak at 27.7° and 12.6° for $O_{1.5}PCN_UPt$ and $O_{2.5}PCN_UPt$ samples remained not notably different, maintaining the strong crystallinity. However, the intensities of these two peaks were decreased in $O_{3.5}PCN_UPt$, suggesting that the CN_U structure can be affected by the decrease of the O ratio in the co-doped process. Additionally, the $O_{3.5}PCN_UPt$ XRD pattern revealed strong Pt peaks at 39.9, 46.4, 67.6, and 81.4°, which were attributed to the (111), (200), (220), and (311) crystal planes, respectively [46]. whereas it was found that the Pt diffraction peaks were slightly less intense in the order of $O_{2.5}PCN_UPt < O_{1.5}PCN_UPt < CN_UPt$. These results imply that Pt can exist in the CN_U structure as a single atom with increasing oxygen doping level and P introduction. However, Pt can grow to a bigger size if there is more oxygen present.

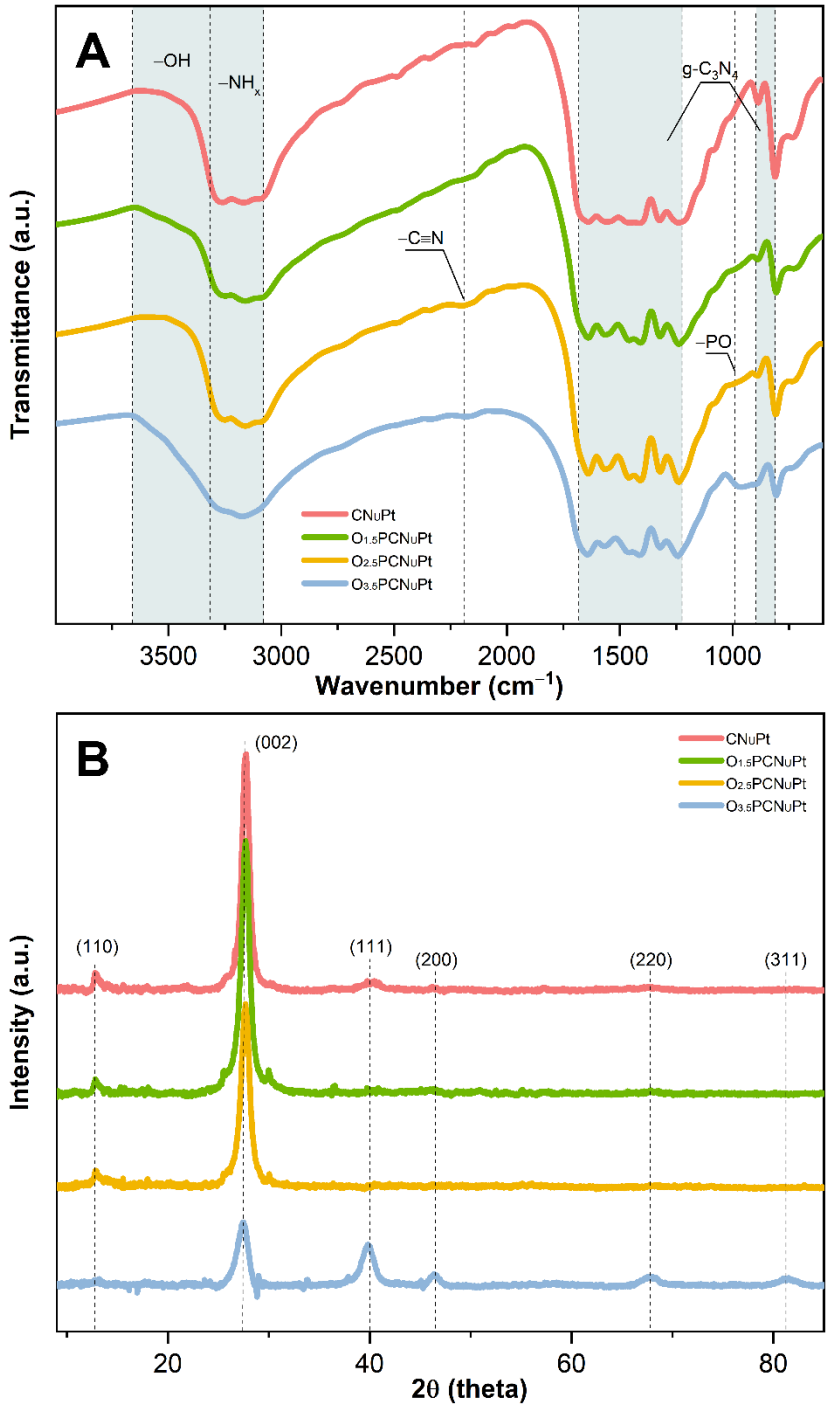

Figure 16. (A) FT-IR spectra and (B) XRD patterns of photocaalysts.

As shown in Figure 17, the morphological structure of photocatalysts was investigated. From the FE-SEM images, CN_UPt (Figure 17a,b) was observed with a clean surface and overlapping lamellar structure of g-C_3N_4. While the co-doped O_yPCN_UPt samples showed small fragments and holes due to the O-doping. Moreover, compared to the layer-by-layer structure of the CN_UPt sample, the $O_{3.5}PCN_UPt$ revealed a hollow and porous structure with numerous structural defects on the surface (Figure 17g,h) due to the increase of the O-doping effect. The high-density Pt distribution of as-prepared samples was illustrated and confirmed in Figure 18 by STEM measurements. A great number of sub-nm atom clusters were determined in addition to single Pt atoms in CN_UPt and $O_{1.5}PCN_UPt$ (Figure 18a,b). Additionally, the homogeneous Pt single atoms were observed in Figure 18c for $O_{2.5}PCN_UPt$. Otherwise, $O_{3.5}PCN_UPt$ revealed a larger Pt nanoparticle size (~1.44 nm), which was consistent with the XRD patterns. The d-spacing of Pt(111) > 0.223nm could be described as the formation of isolated PtO_2 [79].

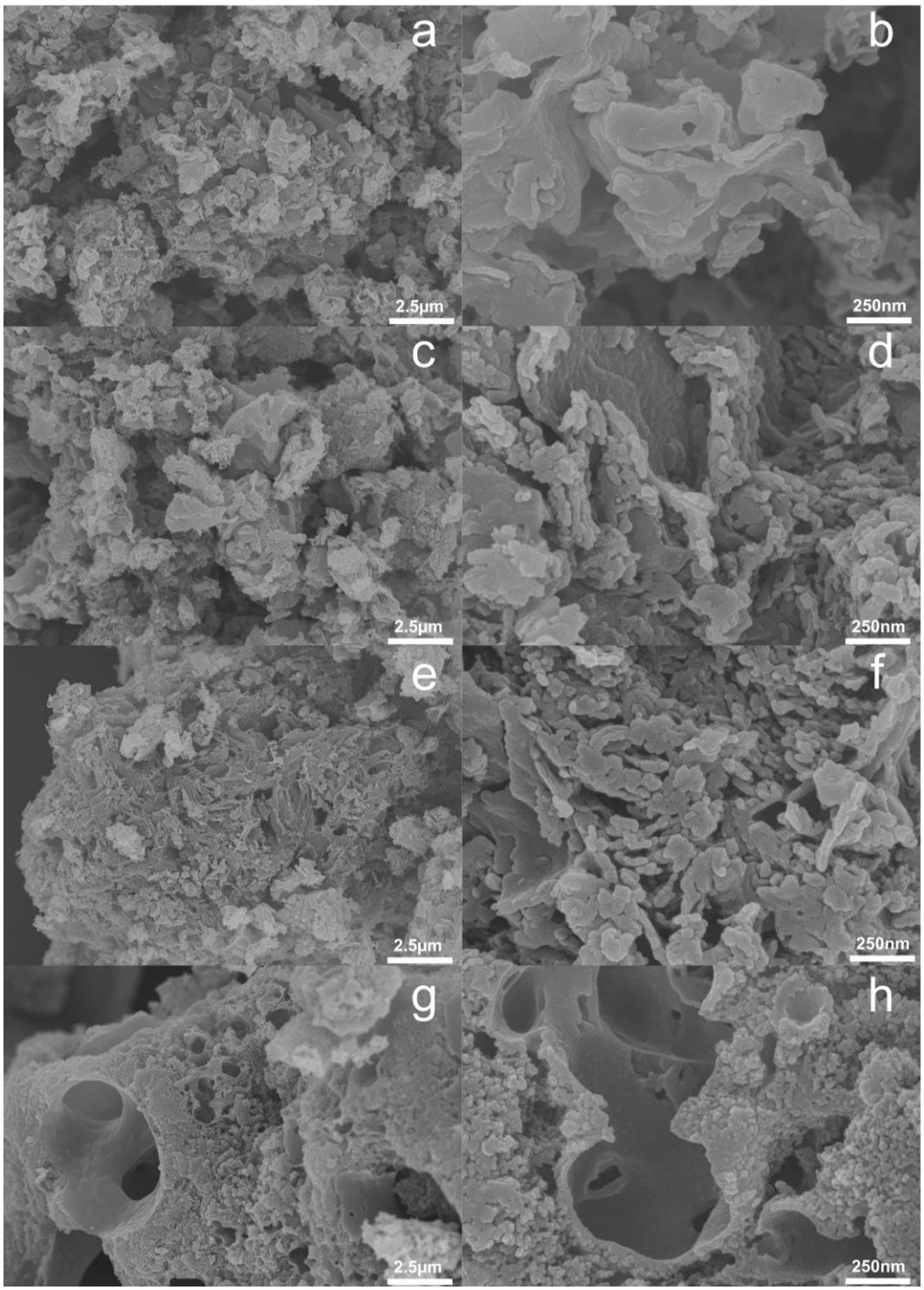

Figure 17. FE-SEM images of CN_UPt (a,b), $O_{1.5}PCN_UPt$ (c,d), $O_{2.5}PCN_UPt$ (e,f), and $O_{3.5}PCN_UPt$ (g,h).

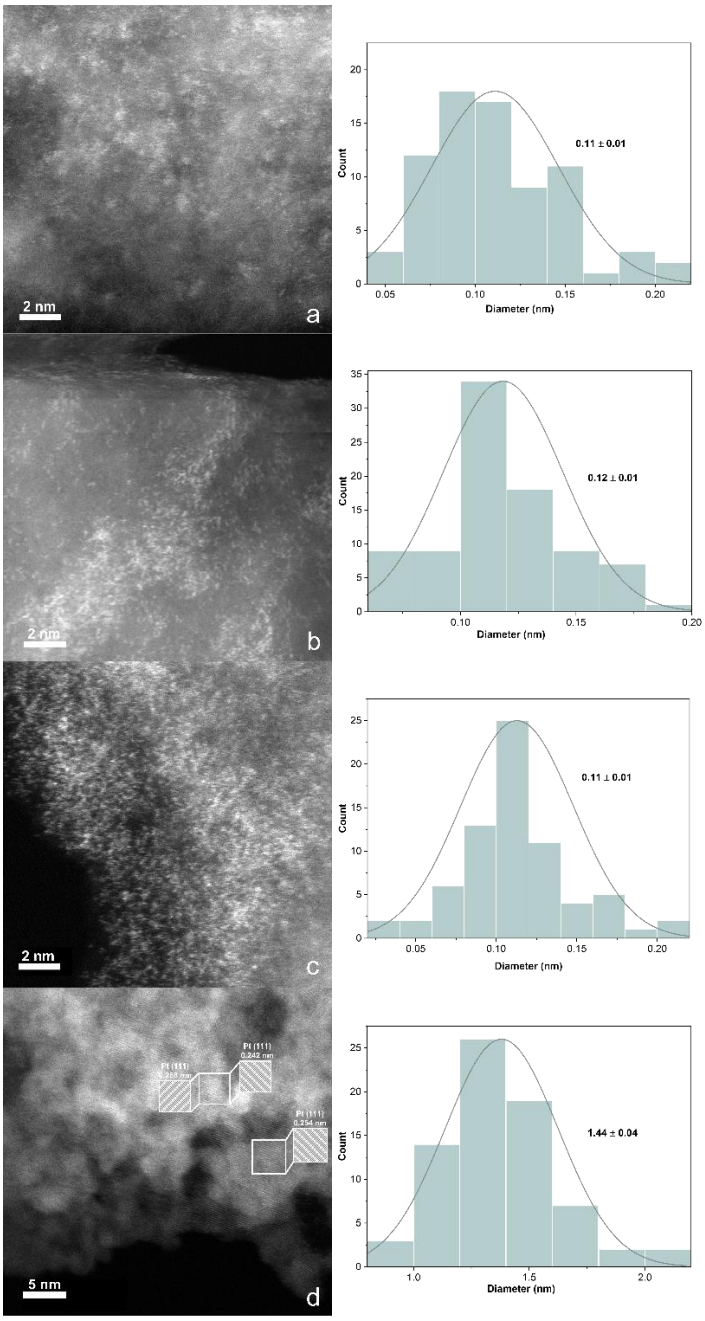

Figure 18. STEM images and Pt diameter (nm) of CN_UPt (a), $O_{1.5}PCN_UPt$ (b), $O_{2.5}PCN_UPt$ (c), and $O_{3.5}PCN_UPt$ (d).

Furthermore, to confirm the composition and the surface chemical state of the following co-doped materials, X-ray photoelectron spectroscopy (XPS) was analyzed and displayed the C 1s, N

1s, C1s, O 1s, P 2p, and Pt 4f, in Figure 19. The surface atomic ratio and atomic percentage of O, P, and Pt were demonstrated and shown in Figure 20. Additionally, evidenced the weight percentage of C, N, O, and Pt, was obtained from the elemental analysis (EA) and an inductively coupled plasma-optical emission spectrometer (ICP-OES). In Figure 19, the C1s spectra showed the peak at 284.5 eV and 288.0 eV, corresponding to the C-C bonding and N–C=N bond, respectively. While the peak displayed at 286.0 eV and 289.0 eV can be deconvoluted for the amino groups (–NHx) and the carboxyl groups (–COOH), respectively [57-60]. The N 1s spectra contained peaks at 401.0, 399.8, and 398.5 eV fitting into the –NHx, N–$(C)_3$, and N_2C (or C–N=C), respectively. Moreover, the doping of O and P demonstrated a new small peak center at around 404.1 eV, which was associated with the localization of positive charge within the heterocycles [33]. The located peaks at 533.0, 532.2, 531.0, and 530.6 eV were assigned to −OH, C=O, PtO, and −COOH, respectively [80]. As demonstrated in Table 5, the O content was increased due to the increase of O_y with the weight percentage increase in the other of $O_{1.5}OCN_UPt < O_{2.5}OCN_UPt < O_{3.5}OCN_UPt$. Furthermore, the increasing atomic ratio of C/O confirmed that O was successfully introduced into the CN_U. The P 2p spectra displayed two typical peaks centered at 134.6 eV and 133.8 eV, indicating the existence of P–Ox bonding and P–C in the O_yPCN_UPt structure [23, 81]. In addition, Pt 4f spectra of photocatalysts were studied with peaks at 71.2 eV and 74.5 eV, relating to metallic Pt (Pt^0) and also confirmed through the XRD results, while Pt^{2+} and Pt^{4+} were observed at 72.7, 76.1, 74.9, and 78.2 eV, respectively [7, 46]. Only Pt^{2+} was shown in the Pt 4f spectra of $O_{2.5}OCN_UPt$, indicating that Pt^{4+} was completely reduced throughout the hydrogen reduction process and confirming the significant interaction between Pt and CN_U.

Table 5. N, C, O, and Pt content (wt.%), and the atomic ratio of photocatalysts.

Samples	wt.%				Atomic ratio		
	N_a	C_a	O_a	Pt_b	P/O_c	C/N_a	O/N_a
CN_UPt	59.7	34.0	4.34	2.70	0.00	0.66	0.13
$O_{1.5}PCN_UPt$	56.6	30.0	5.49	2.80	0.67	0.62	0.18
$O_{2.5}PCN_UPt$	55.6	29.0	7.49	2.35	0.42	0.61	0.26
$O_{3.5}PCN_UPt$	50.0	23.1	11.5	2.27	0.29	0.54	0.50

a: obtains from EA
b: obtains from ICP-OES
c: obtains from XPS

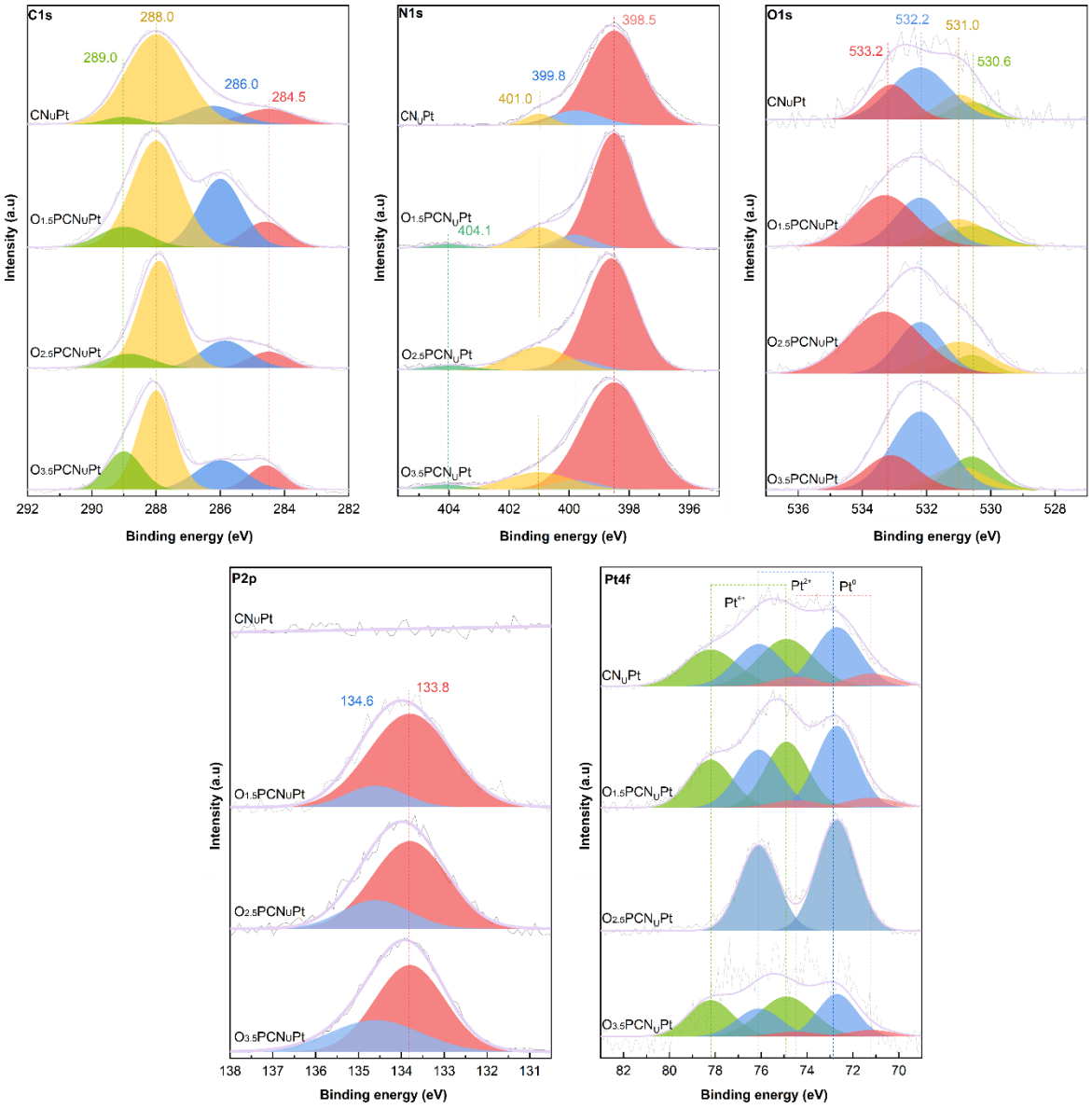

Figure 19. XPS data of C 1s, N 1s, O 1s, P 2p, and Pt 4f for all the photocatalysts.

As shown in Figure 20A, the O-containing functional groups of synthesized samples obtained from O 1s and P 2p were illustrated. The P–Ox groups of photocatalysts significantly increased following to $O_{1.5}PCN_UPt$ < $O_{2.5}PCN_UPt$ < $O_{3.5}PCN_UPt$ (14.3 < 23.0 < 32.3 at.%), due to the increase of O content in the O_yPCN_UPt. Meanwhile, compared to other samples, $O_{2.5}PCN_UPt$ displayed the highest atomic percentage of Pt–O in the order of $O_{2.5}PCN_UPt$ > $O_{1.5}PCN_UPt$ > CN_UPt

> $O_{3.5}PCN_UPt$ (20.0 > 18.7 > 16.6 > 14.1 at.%). From Table 5, the Pt loading content of all photocatalysts was demonstrated to be approximately equal to the initial loading content (3 wt.%). Furthermore, the formation of Pt–O bondings led to the rise of –OH groups in the CN_U structure ($O_{3.5}PCN_UPt$ < CN_UPt < $O_{1.5}PCN_UPt$ < $O_{2.5}PCN_UPt$) as well as the decrease of C=O groups ($O_{3.5}PCN_UPt$ = CN_UPt > $O_{1.5}PCN_UPt$ > $O_{2.5}PCN_UPt$). This revealed that Pt could form the bonding with O in C=O groups, however, the increasing of P–Ox groups number can complete with Pt more than C=O. Figure 20B showed that the content of Pt^{4+} reduced to Pt^{2+} increasing from 45.5 < 50.8 < 100.0 at.% (CN_UPt < $O_{1.5}PCN_UPt$ < $O_{2.5}PCN_UPt$) and the lowest amount of Pt^{2+} was at 40.0 at.% ($O_{3.5}PCN_UPt$). The presence of Pt^{2+} was demonstrated to improve the H_2 evolution production as well as the charge separation efficiency in the photocatalysts structure. These results indicated that during the hydrogen reduction process, the Pt^{4+} could interact with the O_yPCN_U structure to form $Pt^{2+,}$ and $O_{2.5}PCN_UPt$ was expected to be the highest H_2 evolution performance sample owning to its sufficient O and P co-doped CN_U material and highest Pt^{2+} concentration.

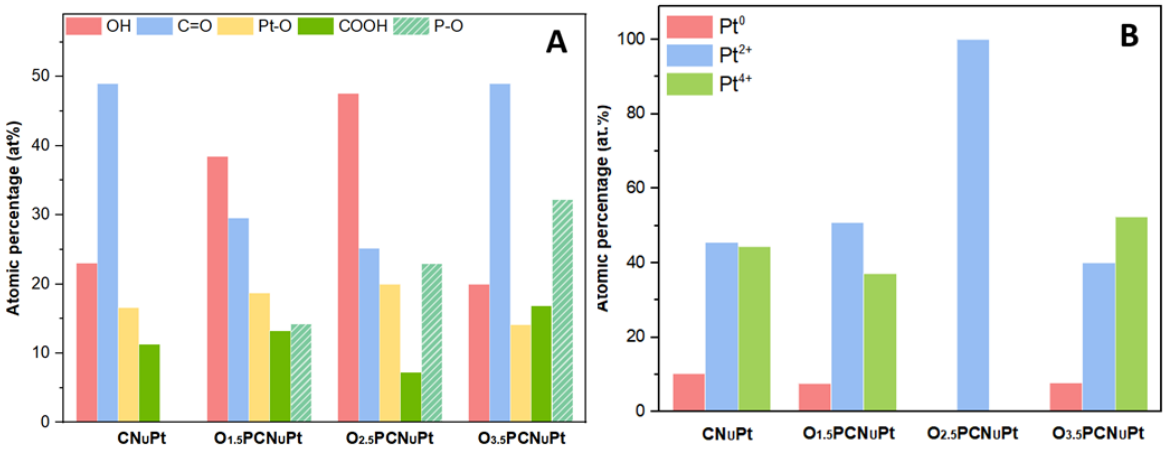

Figure 20. Atomic percentage (at.%) of (A) O-containing functional groups and (B) Pt valence state.

3. 2. 2 Optical properties of modified O_yPCN_UPt

The optical absorption characteristics of the as-prepared samples were examined using the UV-Vis diffuse reflectance spectra (UV-DRS). Figure 21A shows that the absorption edges of CN_UPt, $O_{1.5}PCN_UPt$, $O_{2.5}PCN_UPt$, and $O_{3.5}PCN_UPt$ comprise both the UV and visible light areas and

range from 300 to 600 nm. $O_{2.5}PCN_UPt$ had wide absorption over the visible spectrum, which indicated higher light-harvesting efficiency for the photocatalytic process among all the prepared samples. Additionally, as shown in Figure 21B, the energy band edges (Eg) of the catalysts were estimated using the Tauc plot method. Eg values were determined as 2.70, 2.80, 2.50, and 3.25 eV for CN_UPt, $O_{1.5}PCN_UPt$, $O_{2.5}PCN_UPt$, and $O_{3.5}PCN_UPt$, respectively. The results demonstrate that oxygen and phosphorus co-doping may successfully modify the bandgap of CN_U, which is crucial for enhancing the photocatalytic activity of photocatalysts.

The photoluminescence (PL) spectra show an intensity proportional to the electron-hole recombination rate, which makes them a useful indirect method of estimating the recombination rate of photocatalysts. O_yPCN_UPt catalysts were characterized by PL emission spectra to assess the efficiency of photogenerated electron-hole pair separation, shown in Figure 21C. All of the PL spectra for the OyPCNUPt catalysts in this investigation display two primary emission bands with centers at 435 nm and 460 nm, which is consistent with other studies. The sequence of the emission intensities in the PL spectra is $O_{3.5}PCN_UPt > CN_UPt > O_{1.5}PCN_UPt > O_{2.5}PCN_UPt$, indicating that the lowest emission intensity, which corresponds to the slowest recombination rate, is displayed by $O_{2.5}PCN_UPt$. This result implies that the charge separation and recombination dynamics of the photocatalysts, which are key aspects of the photocatalytic activity, are impacted by co-doping with O and P.

To determine the efficacy of charge separation of photogenerated carriers in photocatalysts, electrochemical impedance spectroscopy (EIS) is a frequently used method. In the EIS plot (Figure 21D), a smaller arc radius indicates a higher charge-transfer efficiency, which is an important factor in overall photocatalytic activity. The arc radius of the semicircle for $O_{2.5}$PCNUPt is less than those for $O_{3.5}PCN_UPt$, CN_UPt, and $O_{1.5}PCN_UPt$, as shown by the Nyquist diagram in Figure 21D, indicating strong conductivity and efficient charge transfer. Notably, a rise of O-containing functional groups was seen along with a steady decrease in the arc radius of O_yPCN_UPt in the order of $CN_UPt > O_{1.5}PCN_UPt > O_{2.5}PCN_UPt$.

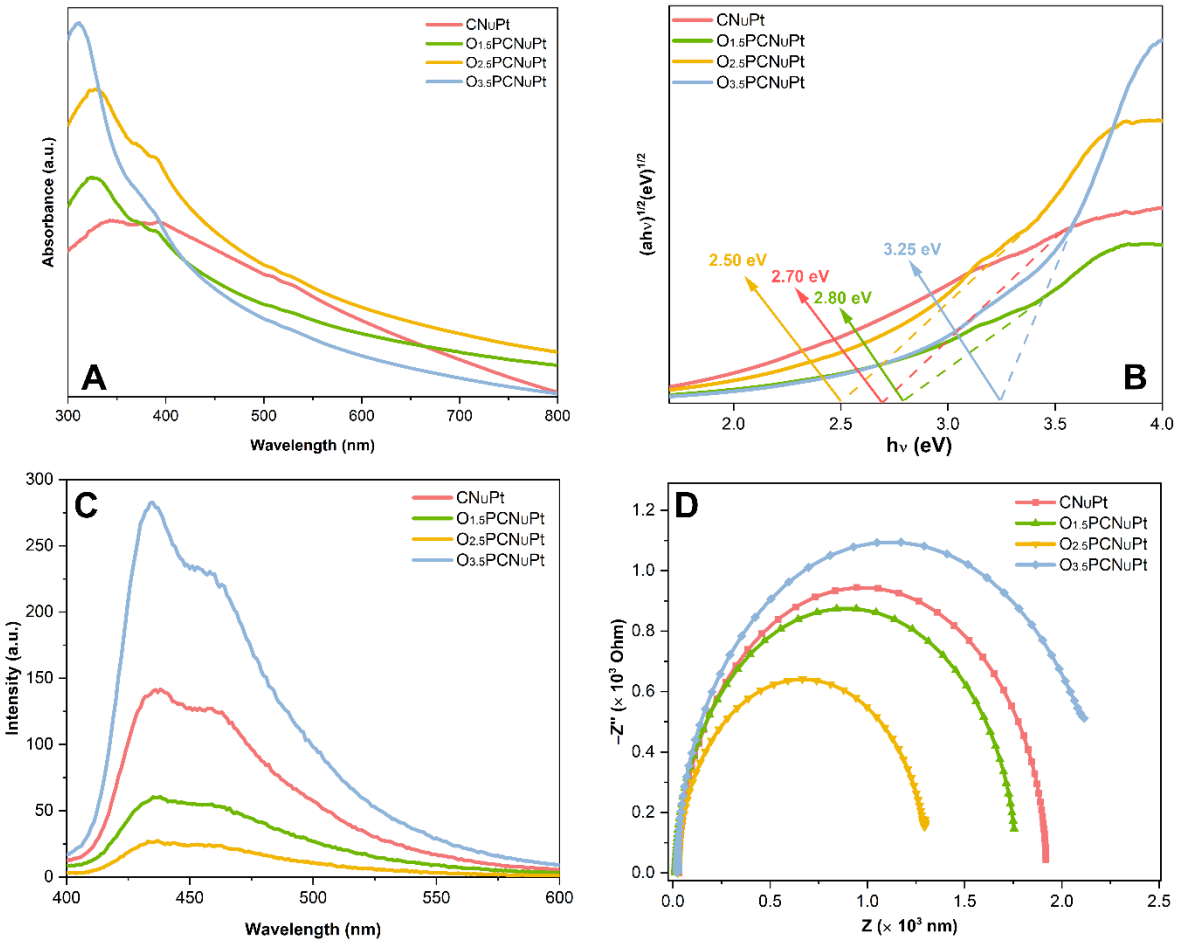

Figure 21. (A) UV–Vis DRS absorption spectra, (B) Tauc plots for the band gap, (C) the PL spectra, and (D) the EIS Nyquist plots of O_yPCN_UPt photocatalysts.

Table 6. Fitted parameters of CN_UPt, $O_{1.5}PCN_UPt$, $O_{2.5}PCN_UPt$, and $O_{3.5}PCN_UPt$ for the Nyquist plots.

Fitted parameters	CN_UPt	$O_{1.5}PCN_UPt$	$O_{2.5}PCN_UPt$	$O_{3.5}PCN_UPt$
R_s (Ohm)	29.59	14.95	26.08	22.57
R_{ct} (Ohm)	1890	1752	1282	2190
C_1 (F)	5.91×10^{-6}	2.05×10^{-6}	7.50×10^{-6}	8.25×10^{-6}
C_2 (F)	-0.02×10^{-3}	-1.00×10^{-3}	2.08×10^{3}	0.56×10^{3}

In addition, as shown in Figure 22A, the VB of the CN_UPt, $O_{1.5}PCN_UPt$, $O_{2.5}PCN_UPt$, and $O_{3.5}PCN_UPt$ were determined as 1.5, 1.6, 1.5, and 2.1 eV, respectively, by the XPS-VB. The theoretical CB position was computed at –1.20, –1.20, –1.00, –1.15 eV using equation (3). In Figure 22B, the band structure diagram of all photocatalysts was illustrated. The results indicated that the production of H_2 through the reduction of H^+ was feasible since the synthesized samples had a beneficial potential. Furthermore, it was possible that the highly negative position of the CB of $O_{2.5}PCN_UPt$ could assist with the greater H_2 evolution reaction in an aqueous environment, which agreed with the PL and EIS results.

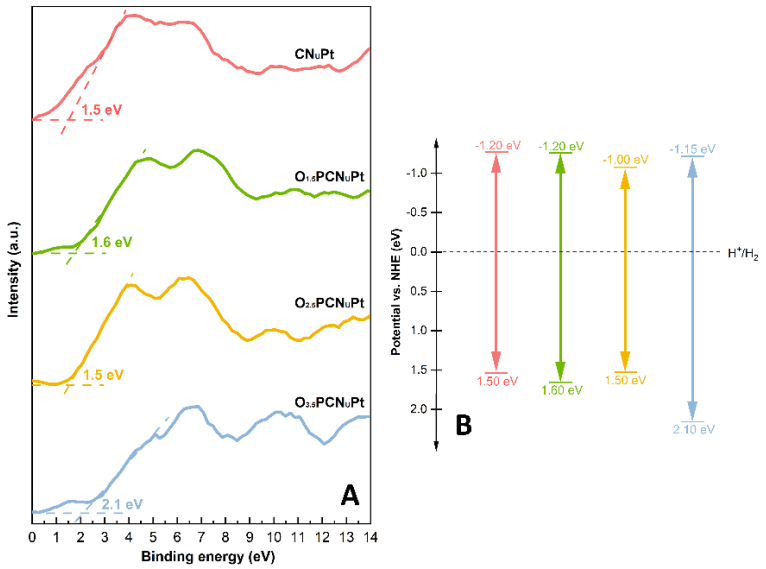

Figure 22. (A) XPS-VB spectra and (B) band structure diagram of the synthesized samples.

3. 2. 3 H_2 evolution performance

As shown in Figure 23A, the photocatalytic H_2 evolution over time for all the O_yPCN_UPt catalysts was illustrated. A higher H_2 evolution rate was observed for $O_{1.5}PCN_UPt$ and $O_{2.5}PCN_UPt$ than for CN_UPt, while a lower rate was observed for $O_{3.5}PCN_UPt$. The highest H_2 evolution production was $O_{2.5}PCN_UPt$ at 2198 μmol. g^{-1}. The CN_UPt, $O_{1.5}PCN_UPt$, and $O_{3.5}PCN_UPt$ manifested H_2 evolution production of 1330, 1464, and 1190 μmol. g^{-1}, respectively. Besides that, the H_2 evolution rate of all the photocatalysts was shown in Figure 23B in the order of $O_{2.5}PCN_UPt$ > $O_{1.5}PCN_UPt$ > CN_UPt > $O_{3.5}PCN_UPt$ (439.7 > 292.7 > 265.9 > 238.0 μmol. g^{-1}. h^{-1}, respectively). According to these results, co-doping with oxygen and phosphorus enhances the photocatalytic activity of CN_U for hydrogen evolution reactions. A synergistic effect was demonstrated between Oxygen and Phosphorus co-doping to produce the highest H_2 evolution production and rate for $O_{2.5}PCN_UPt$. By introducing oxygen and phosphorus into the CN_U lattice, defect sites can be introduced and the electronic structure of the photocatalyst may be modified, improving charge transfer and separation efficiency. It is also suggested that the photocatalytic activity is determined by the concentration of the co-dopants, with a maximum rate of H_2 evolution when O and P are in optimum concentrations. Besides that, the photocatalytic stability of $O_{2.5}PCN_UPt$ through three runs was investigated and shown in Figure 23C. The result revealed that the H_2 production remained constant after the third run, indicating exceptional photocatalytic stability and reusability for visible-light-driven H_2 generation.

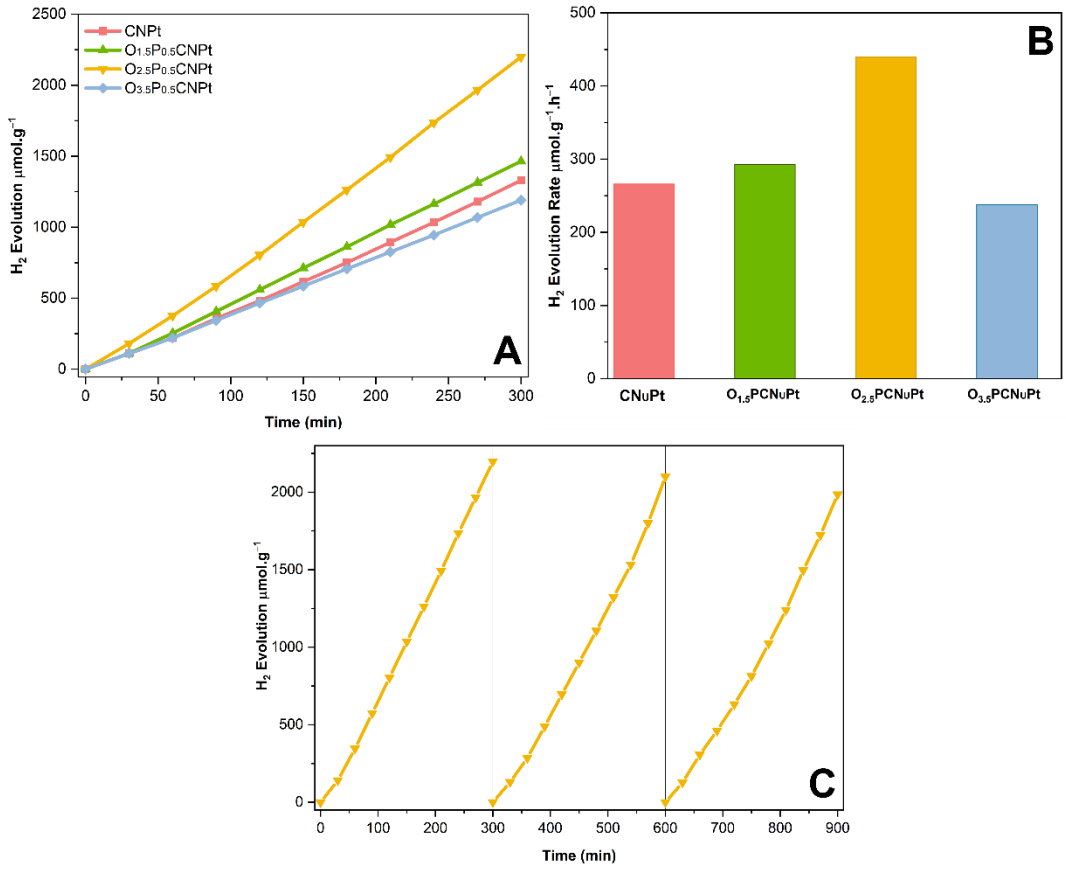

Figure 23. (A) Hydrogen evolution performance (µmol. g^{-1}), (B) Hydrogen evolution rate (µmol. $g^{-1}.h^{-1}$) of O_yPCN_UPt, and (C) recycle test of $O_{2.5}PCN_UPt$.

With the results gained above, the chemical structure of CN_UPt, $O_{2.5}PCN_UPT$, and $O_{3.5}PCN_UPt$ before and after the Pt loading process were illustrated in Figure 24. In the CN_UPt, $Pt^{2+,}$ and Pt^{4+} were formed with the PtO and Pt-N coordination bonds without the existence of a P-doping element [46, 82]. Whereas, the Pt^{4+} in the $O_{3.5}PCN_UPt$ was significantly transformed to the isolated PtO_2, as confirmed by the STEM images. Additionally, through the XPS data and STEM results, the homogeneous Pt^{2+} single atoms were generated owing to an ideal O/P doping ratio. The homogeneous Pt single atoms led to the effective charge transfer, resulting in the highest H_2 evolution rate.

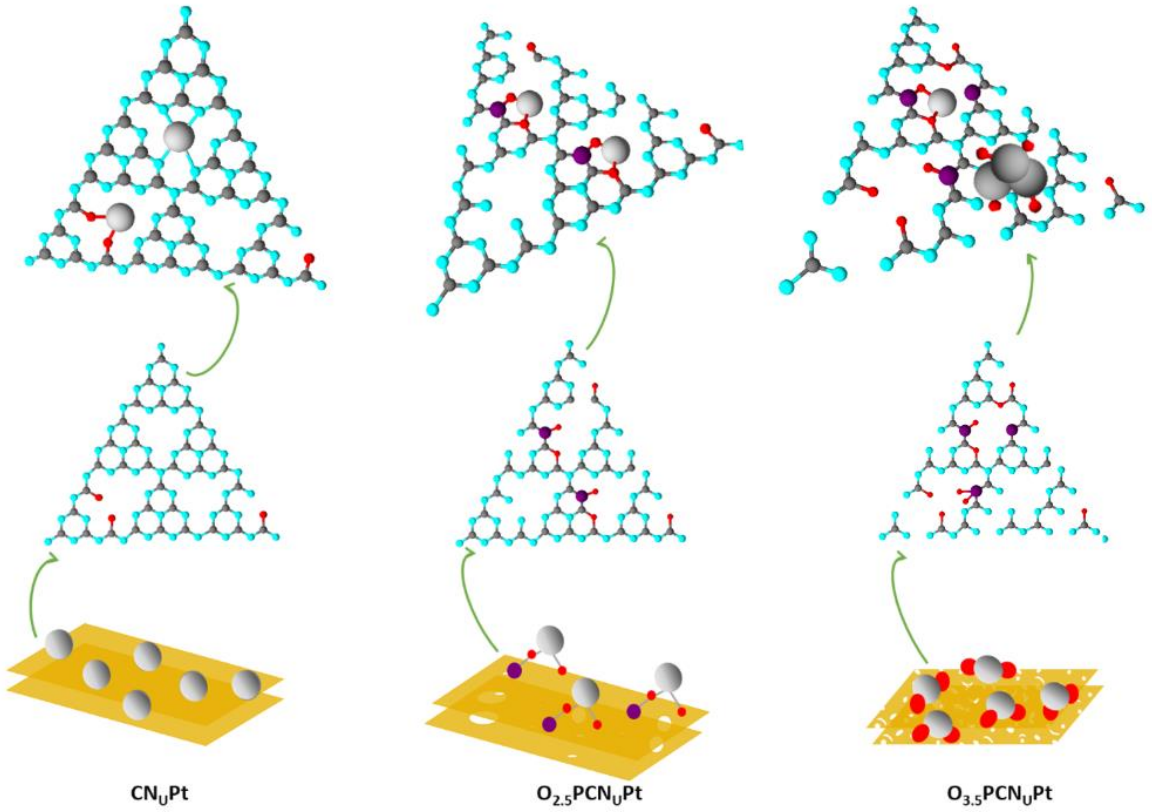

Figure 24. A schematic formation of CNuPt, $O_{2.5}PCN_UPt$, and $O_{3.5}PCN_UPt$ (before and after Pt loading).

3. 2. 4 Conclusion

In conclusion, a one-step calcination process was successfully employed co-doped O and P into the CN_U structure. It had been confirmed that the co-doped materials could enhance the photocatalytic activity via lower the energy band gap, improving the charge separation, and preventing the recombination of electron-hole pairs. Furthermore, by the effect of O and P co-doped, the Pt was facilitated to form the Pt^{2+}, which promoted the H_2 evolution production. As a result, the most appropriate O-doping content, $O_{2.5}PCN_UPt$, revealed the greatest H_2 evolution rate at 439.7 μmol $g^{-1}h^{-1}$.

Chapter 4. CONCLUSION

After using various surface modification processes to enhance the photocatalytic activity of g-C_3N_4, the thesis can be concluded as:

The effectiveness of hydrothermal treatment on CN in the photodegradation of TC under various circumstances was investigated in the first study. The hydrothermal treatment sufficiently added O-containing groups to CN and the formation extended melem units on CN at the same time, which hindered the charge separation efficiency. With a rate of 97.17%, CN-180-6 demonstrated among the studied samples the best effectiveness in TC decomposition under visible light irradiation. This was owing to CN-180-6 having the largest specific surface area since it has more O-functional groups in general and less extended melem units specifically on CN.

Hydrothermal treatment could introduce more O-containing functional groups into the g-C_3N_4 structure, however, the longer hydrothermal time could lead to the extension of melem units, which had a negative effect on the photocatalytic performance of g-C_3N_4. Since the O and P co-doped g-C_3N_4 through a one-step calcined process could inhibit the formation of melem units and control the O-doping concentration. Moreover, O_yPCN_UPt materials could narrow the bandgap structure, advance the charge separation, suppress the recombination of electrons, and especially facilitate the reduction of Pt^{4+} to Pt^{2+} during the hydrogen reduction procedure to improve photocatalytic production. Consequently, the $O_{2.5}PCN_UPt$ manifested the highest H_2 evolution rate at 439.7 μmol g^{-1} h^{-1} due to the sufficient O and P co-doped content.

References

1. Zhang, M., et al., *A critical review of g-C_3N_4-based photocatalytic membrane for water purification.* Chemical Engineering Journal, 2021. 412: p. 128663.

2. Reddy, K.R., et al., *Polymeric graphitic carbon nitride (g-C_3N_4)-based semiconducting nanostructured materials: synthesis methods, properties and photocatalytic applications.* Journal of environmental management, 2019. 238: p. 25-40.

3. Li, Y., et al., *Design and application of active sites in g-C_3N_4-based photocatalysts.* Journal of Materials Science & Technology, 2020. 56: p. 69-88.

4. Inagaki, M., et al., *Graphitic carbon nitrides (g-C_3N_4) with comparative discussion to carbon materials.* Carbon, 2019. 141: p. 580-607.

5. Nguyen, T.K.A., et al., *Defect engineering of water-dispersible g-C_3N_4 photocatalysts by chemical oxidative etching of bulk g-C_3N_4 prepared in different calcination atmospheres.* Journal of Materials Science & Technology, 2022. 103: p. 232-243.

6. Qin, Y., et al., *Synergy between van der waals heterojunction and vacancy in $ZnIn_2S_4$/g-C_3N_4 2D/2D photocatalysts for enhanced photocatalytic hydrogen evolution.* Applied Catalysis B: Environmental, 2020. 277: p. 119254.

7. Hoang, T.V.A., et al., *Solvent Etching Process for Graphitic Carbon Nitride Photocatalysts Containing Platinum Cocatalyst: Effects of Water Hydrolysis on Photocatalytic Properties and Hydrogen Evolution Behaviors.* Nanomaterials, 2022. 12(7): p. 1188.

8. Zhu, D. and Q. Zhou, *Nitrogen doped g-C_3N_4 with the extremely narrow band gap for excellent photocatalytic activities under visible light.* Applied Catalysis B: Environmental, 2021. 281: p. 119474.

9. Zeng, Y., et al., *Sea-urchin-structure g-C_3N_4 with narrow bandgap (~ 2.0 eV) for efficient overall water splitting under visible light irradiation.* Applied Catalysis B: Environmental, 2019. 249: p. 275-281.

10. Gan, J., et al., *Efficient synthesis of tunable band-gap CuInZnS decorated g-C_3N_4 hybrids for enhanced CO_2 photocatalytic reduction and near-infrared-triggered photodegradation performance.* Applied Surface Science, 2021. 564: p. 150396.

11. Ong, W.-J., et al., *Graphitic carbon nitride (g-C_3N_4)-based photocatalysts for artificial photosynthesis and environmental remediation: are we a step closer to achieving sustainability?* Chemical reviews, 2016. 116(12): p. 7159-7329.

12. Wang, A., et al., *Recent advances of graphitic carbon nitride-based structures and applications in catalyst, sensing, imaging, and LEDs.* Nano-micro letters, 2017. 9: p. 1-21.

13. Liu, X., et al., *Recent developments of doped g-C_3N_4 photocatalysts for the degradation of organic pollutants.* Critical Reviews in Environmental Science and Technology, 2021. 51(8): p. 751-790.

14. Feng, D., et al., *Enhanced photocatalytic activities of g-C_3N_4 with large specific surface area via a facile one-step synthesis process.* Carbon, 2017. 125: p. 454-463.

15. Liang, L., et al., *g-C_3N_4 nano-fragments as highly efficient hydrogen evolution photocatalysts: boosting effect of nitrogen vacancy.* Applied Catalysis A: General, 2020. 599: p. 117618.

16. Ye, X., et al., *Revealing the transfer mechanisms of photogenerated charge carriers over g-C_3N_4/$ZnIn_2S_4$ composite: a model study for photocatalytic oxidation of aromatic alcohols with visible light.* Journal of Catalysis, 2021. 401: p. 149-159.

17. Bu, X., et al., *Surface modification of g-C_3N_4 through oxygen-plasma treatment: a simple way toward excellent hydrophilicity.* ACS Applied Materials & Interfaces, 2016. 8(45): p. 31419-31425.

18. Zhu, B., et al., *H_2O molecule adsorption on s-triazine-based g-C_3N_4.* Chinese Journal of Catalysis, 2021. 42(1): p. 115-122.

19. Peng, X., et al., *Construction of a Z-scheme g-C_3N_4/NBGO/$BiVO_4$ heterostructure with visible-light driven photocatalytic degradation of tetracycline: efficiency, reaction pathway and mechanism.* Catalysis Science & Technology, 2022. 12(4): p. 1339-1358.

20. Huang, H., et al., *The heterojunction construction of hybrid B-doped g-C_3N_4 nanosheets and ZIF67 by simple mechanical grinding for improved photocatalytic hydrogen evolution.* International Journal of Hydrogen Energy, 2023.

21. Tay, Q., et al., *Defect engineered g-C_3N_4 for efficient visible light photocatalytic hydrogen production.* Chemistry of Materials, 2015. 27(14): p. 4930-4933.

22. Kumar, A., et al., *C-, N-Vacancy defect engineered polymeric carbon nitride towards photocatalysis: viewpoints and challenges.* Journal of Materials Chemistry A, 2021. 9(1): p. 111-153.

23. Li, W., et al., *Facile in situ reductive synthesis of both nitrogen deficient and protonated g-C_3N_4 nanosheets for the synergistic enhancement of visible-light H_2 evolution.* Chemical Science, 2020. 11(10): p. 2716-2728.

24. Liu, Z., et al., *Phosphorus and sulphur co-doping of g-C_3N_4 nanotubes with tunable architectures for superior photocatalytic H_2 evolution.* International Journal of Hydrogen Energy, 2019. 44(36): p. 20042-20055.

25. Du, R., et al., *Controlled oxygen doping in highly dispersed Ni-loaded g-C_3N_4 nanotubes for efficient photocatalytic H_2O_2 production.* Chemical Engineering Journal, 2022: p. 135999.

26. Prasad, C., et al., *A latest overview on photocatalytic application of g-C_3N_4 based nanostructured materials for hydrogen production.* international journal of hydrogen energy, 2020. 45(1): p. 337-379.

27. Zhang, Y., et al., *Activation of carbon nitride solids by protonation: morphology changes, enhanced ionic conductivity, and photoconduction experiments.* Journal of the American Chemical Society, 2009. 131(1): p. 50-51.

28. Yang, X., et al., *Tuning the morphology of g-C_3N_4 for improvement of Z-scheme photocatalytic water oxidation.* ACS applied materials & interfaces, 2015. 7(28): p. 15285-15293.

29. Wang, Y., et al., *3D network-like rGO-$MoSe_2$ modified g-C_3N_4 nanosheets with Z-scheme heterojunction: Morphology control, heterojunction construct, and boosted photocatalytic performances.* Journal of Alloys and Compounds, 2022. 897: p. 163197.

30. Hou, L., et al., *Flower-Like Dual-Defective Z-Scheme Heterojunction g-C_3N_4/$ZnIn_2S_4$ High-Efficiency Photocatalytic Hydrogen Evolution and Degradation of Mixed Pollutants.* Nanomaterials, 2021. 11(10): p. 2483.

31. Song, T., et al., *3D reticulated carbon nitride materials high-uniformly capture 0D black phosphorus as 3D/0D composites for stable and efficient photocatalytic hydrogen evolution.* Journal of Materials Chemistry A, 2019. 7(2): p. 503-512.

32. Lei, L., et al., *Surface-assisted synthesis of biomass carbon-decorated polymer carbon nitride for efficient visible light photocatalytic hydrogen evolution.* Journal of Colloid and Interface Science, 2023. 634: p. 1014-1023.

33. Jiang, Y., et al., *Enhancement of photocatalytic hydrogen evolution activity of porous oxygen doped g-C_3N_4 with nitrogen defects induced by changing electron transition.* Applied Catalysis B: Environmental, 2019. 240: p. 30-38.

34. Wang, J., et al., *A porous g-C_3N_4 nanosheets containing nitrogen defects for enhanced photocatalytic removal meropenem: Mechanism, degradation pathway and DFT calculation.* Environmental Research, 2020. 184: p. 109339.

35. Zhu, Y., et al., *A [001]-Oriented Hittorf's Phosphorus Nanorods/Polymeric Carbon Nitride Heterostructure for Boosting Wide-Spectrum-Responsive Photocatalytic Hydrogen Evolution from Pure Water.* Angewandte Chemie International Edition, 2020. 59(2): p. 868-873.

36. Murray, C.J., et al., *Global burden of bacterial antimicrobial resistance in 2019: a systematic analysis.* The Lancet, 2022. 399(10325): p. 629-655.

37. Peng, X., et al., *Evaluation of degradation behavior over tetracycline hydrochloride by microbial electrochemical technology: Performance, kinetics, and microbial communities.* Ecotoxicology and Environmental Safety, 2020. 188: p. 109869.

38. De Cazes, M., et al., *Design and optimization of an enzymatic membrane reactor for tetracycline degradation.* Catalysis Today, 2014. 236: p. 146-152.

39. Zhi, D., et al., *Development of ozonation and reactive electrochemical membrane coupled process: Enhanced tetracycline mineralization and toxicity reduction.* Chemical Engineering Journal, 2020. 383: p. 123149.

40. Shao, S. and X. Wu, *Microbial degradation of tetracycline in the aquatic environment: a review.* Critical reviews in biotechnology, 2020. 40(7): p. 1010-1018.

41. Fattahimoghaddam, H., T. Mahvelati-Shamsabadi, and B.-K. Lee, *Efficient photodegradation of rhodamine B and tetracycline over robust and green g-C_3N_4 nanostructures: supramolecular design.* Journal of Hazardous Materials, 2021. 403: p. 123703.

42. Si, Q., et al., *Difunctional carbon quantum dots/g-C_3N_4 with in-plane electron buffer for intense tetracycline degradation under visible light: Tight adsorption and smooth electron transfer.* Applied Catalysis B: Environmental, 2021. 299: p. 120694.

43. IEA, *Key World Energy Statistics 2021*. 2021.

44. Banos, R., et al., *Optimization methods applied to renewable and sustainable energy: A review.* Renewable and sustainable energy reviews, 2011. 15(4): p. 1753-1766.

45. Zhu, Q., et al., *Emerging cocatalysts on g-C_3N_4 for photocatalytic hydrogen evolution.* Small, 2021. 17(40): p. 2101070.

46. Nguyen, P.A., et al., *Highly dispersed PtO over g-C_3N_4 by specific metal-support interactions and optimally distributed Pt species to enhance hydrogen evolution rate of Pt/g-C_3N_4 photocatalysts.* Chemical Engineering Journal, 2023. 464: p. 142765.

47. Zhang, G., et al., *An ingenious strategy of preparing TiO_2/g-C_3N_4 heterojunction photocatalyst: In situ growth of TiO_2 nanocrystals on g-C_3N_4 nanosheets via impregnation-calcination method.* Applied Surface Science, 2018. 433: p. 963-974.

48. Wu, Z., et al., *MXene Ti_3C_2 derived Z–scheme photocatalyst of graphene layers anchored TiO_2/g–C_3N_4 for visible light photocatalytic degradation of refractory organic pollutants.* Chemical Engineering Journal, 2020. 394: p. 124921.

49. Ge, L., C. Han, and J. Liu, *Novel visible light-induced g-C_3N_4/Bi_2WO_6 composite photocatalysts for efficient degradation of methyl orange.* Applied Catalysis B: Environmental, 2011. 108: p. 100-107.

50. Liu, D., et al., *ZIF-67-Derived 3D Hollow Mesoporous Crystalline Co_3O_4 Wrapped by 2D g-C_3N_4 Nanosheets for Photocatalytic Removal of Nitric Oxide.* Small, 2019. 15(31): p. 1902291.

51. Wang, Y., et al., *Effect of nonmetal element dopants on photo-and electro-chemistry performance of ultrathin g-C_3N_4 nanosheets.* International Journal of Hydrogen Energy, 2020. 45(33): p. 16519-16527.

52. Xiao, P., et al., *Construction of RGO/$CdIn_2S_4$/g-C_3N_4 ternary hybrid with enhanced photocatalytic activity for the degradation of tetracycline hydrochloride.* Applied Surface Science, 2018. 433: p. 388-397.

53. Ming, L., et al., *Hydrothermal synthesis of oxidized g-C_3N_4 and its regulation of photocatalytic activity.* Journal of materials chemistry A, 2014. 2(45): p. 19145-19149.

54. Zhang, S., et al., *Enhanced photodegradation of toxic organic pollutants using dual-oxygen-doped porous g-C_3N_4: Mechanism exploration from both experimental and DFT studies.* Applied Catalysis B: Environmental, 2019. 248: p. 1-10.

55. Lv, S.-W., et al., *MOF-derived $CoFe_2O_4$/Fe_2O_3 embedded in g-C_3N_4 as high-efficient Z-scheme photocatalysts for enhanced degradation of emerging organic pollutants in the presence of persulfate.* Separation and Purification Technology, 2020. 253: p. 117413.

56. Zhou, D., et al., *Improved visible light photocatalytic activity on Z-scheme g-C_3N_4 decorated TiO_2 nanotube arrays by a simple impregnation method.* Materials Research Bulletin, 2020. 124: p. 110757.

57. Wang, W., et al., *Sulfur doped carbon quantum dots loaded hollow tubular g-C_3N_4 as novel photocatalyst for destruction of Escherichia coli and tetracycline degradation under visible light.* Chemical Engineering Journal, 2019. 378: p. 122132.

58. Li, Y., et al., *Construction of g-C_3N_4/PDI@ MOF heterojunctions for the highly efficient visible light-driven degradation of pharmaceutical and phenolic micropollutants.* Applied Catalysis B: Environmental, 2019. 250: p. 150-162.

59. Zhou, Y., et al., *Brand new P-doped g-C_3N_4: enhanced photocatalytic activity for H_2 evolution and Rhodamine B degradation under visible light.* Journal of Materials Chemistry A, 2015. 3(7): p. 3862-3867.

60. Samanta, S., et al., *Surface modified C, O co-doped polymeric g-C_3N_4 as an efficient photocatalyst for visible light assisted CO_2 reduction and H_2O_2 production.* Applied Catalysis B: Environmental, 2019. 259: p. 118054.

61. Khaing, K.K., et al., *Efficient solar light driven degradation of tetracycline by Fe-EDTA modified g-C_3N_4 nanosheets.* The Journal of Physical Chemistry C, 2020. 124(22): p. 11831-11843.

62. Fu, J., et al., *Hierarchical porous O-doped g-C_3N_4 with enhanced photocatalytic CO_2 reduction activity.* Small, 2017. 13(15): p. 1603938.

63. Cui, L., et al., *Facile preparation of Z-scheme WO_3/g-C_3N_4 composite photocatalyst with enhanced photocatalytic performance under visible light.* Applied Surface Science, 2017. 391: p. 202-210.

64. Lu, N., et al., *Characterization of highly effective plasma-treated g-C_3N_4 and application to the photocatalytic H_2O_2 production.* Chemosphere, 2020. 241: p. 124927.

65. Li, Y., et al., *Enhancing the photocatalytic activity of bulk g-C_3N_4 by introducing mesoporous structure and hybridizing with graphene.* Journal of colloid and interface science, 2014. 436: p. 29-36.

66. Wang, X., et al., *A facile hydrothermal synthesis of carbon dots modified g-C_3N_4 for enhanced photocatalytic H_2-evolution performance.* Dalton Transactions, 2017. 46(19): p. 6417-6424.

67. Tang, H., et al., *Oxygen doped g-C_3N_4 with nitrogen vacancy for enhanced photocatalytic hydrogen evolution.* Chemistry–An Asian Journal, 2020. 15(21): p. 3456-3461.

68. Chen, H., et al., *A facile and green microwave hydrothermal method for fabricating g-C_3N_4 nanosheets with improved hydrogen evolution performance.* Journal of Alloys and Compounds, 2021. 863: p. 158448.

69. Zhu, P., et al., *High visible light response Z-scheme $Ag_3PO_4/g\text{-}C_3N_4/ZnO$ composite photocatalyst for efficient degradation of tetracycline hydrochloride: preparation, properties and mechanism.* Journal of Alloys and Compounds, 2020. 840: p. 155714.

70. Jiang, L., et al., *Metal-free efficient photocatalyst for stable visible-light photocatalytic degradation of refractory pollutant.* Applied Catalysis B: Environmental, 2018. 221: p. 715-725.

71. Tang, W., et al., *Supramolecular copolymerization strategy for realizing the broadband white light luminescence based on N-deficient porous graphitic carbon nitride ($g\text{-}C_3N_4$).* ACS applied materials & interfaces, 2020. 12(5): p. 6396-6406.

72. Putri, L.K., et al., *Insights on the impact of doping levels in oxygen-doped $g\text{-}C_3N_4$ and its effects on photocatalytic activity.* Applied Surface Science, 2020. 504: p. 144427.

73. Zeng, Y., et al., *Scalable one-step production of porous oxygen-doped $g\text{-}C_3N_4$ nanorods with effective electron separation for excellent visible-light photocatalytic activity.* Applied Catalysis B: Environmental, 2018. 224: p. 1-9.

74. Li, Y., et al., *Enhanced photocatalytic H_2-production activity of C-dots modified $g\text{-}C_3N_4/TiO_2$ nanosheets composites.* Journal of colloid and interface science, 2018. 513: p. 866-876.

75. Wang, D., et al., *In-situ growth of $\beta\text{-}Bi_2O_3$ nanosheets on $g\text{-}C_3N_4$ to construct direct Z-scheme heterojunction with enhanced photocatalytic activities.* Journal of Alloys and Compounds, 2021. 859: p. 157795.

76. Hong, Y., et al., *Efficient and stable Nb_2O_5 modified $g\text{-}C_3N_4$ photocatalyst for removal of antibiotic pollutant.* Chemical Engineering Journal, 2016. 299: p. 74-84.

77. Jiang, L., et al., *Nitrogen self-doped $g\text{-}C_3N_4$ nanosheets with tunable band structures for enhanced photocatalytic tetracycline degradation.* Journal of colloid and interface science, 2019. 536: p. 17-29.

78. Bekiaris, G., et al., *Using FTIR-photoacoustic spectroscopy for phosphorus speciation analysis of biochars.* Spectrochimica Acta Part A: Molecular and Biomolecular Spectroscopy, 2016. 168: p. 29-36.

79. Fuchs, T., et al., *Structure dependency of the atomic-scale mechanisms of platinum electro-oxidation and dissolution.* Nature Catalysis, 2020. 3(9): p. 754-761.

80. Hoang, T.V.A., P.A. Nguyen, and E.W. Shin, *Effect of Morphological Modification over g-C_3N_4 on Photocatalytic Hydrogen Evolution Performance of g-C_3N_4-Pt Photocatalysts.* Catalysts, 2023. 13(1): p. 92.

81. Rumble Jr, J., D. Bickham, and C. Powell, *The NIST x-ray photoelectron spectroscopy database.* Surface and interface analysis, 1992. 19(1-12): p. 241-246.

82. Ding, J., et al., *Plasma synthesis of Pt/g-C_3N_4 photocatalysts with enhanced photocatalytic hydrogen generation.* Journal of Alloys and Compounds, 2021. 873: p. 159871.